CrossMark

Radio Morphology of Gamma-Ray Sources: Double-lobed Radio Sources

Vaidehi S. Paliya[1] , D. J. Saikia[1] , Alberto Domínguez[2] , and C. S. Stalin[3]

[1] Inter-University Centre for Astronomy and Astrophysics (IUCAA), SPPU Campus, Pune 411007, India; vaidehi.s.paliya@gmail.com
[2] IPARCOS and Department of EMFTEL, Universidad Complutense de Madrid, E-28040 Madrid, Spain
[3] Indian Institute of Astrophysics, Block II, Koramangala, Bengaluru 560034, Karnataka, India

Abstract

The extragalactic γ-ray sky is dominated by relativistic jets aligned to the observer's line of sight, i.e., blazars. A few of their misaligned counterparts, e.g., radio galaxies, are also detected with the Fermi-Large Area Telescope (LAT), albeit in a small number ($\sim$50), indicating the crucial role played by the jet viewing angle in detecting γ-ray emission from jets. These γ-ray emitting misaligned active galactic nuclei (AGN) provide us with a unique opportunity to understand the high-energy emission production mechanisms from a different viewpoint than the more common blazars. With this goal in mind, we have systematically studied the radio morphology of γ-ray emitting sources present in the fourth data release of the fourth catalog of Fermi-LAT detected γ-ray sources to identify misaligned AGN. By utilizing the high-resolution and sensitive MHz and GHz frequency observations delivered by the Very Large Array Sky Survey, Low-Frequency Array Two-metre Sky Survey, Faint Images of the Radio Sky at Twenty Centimeters, and Rapid ASKAP Continuum Survey, here we present a catalog of 149 γ-ray detected misaligned AGN, thus approximately tripling the number of known objects of this class. Our sample includes a variety of radio morphologies, e.g., edge-darkened and edge-brightened, hybrids, wide-angle-tailed, bent jets, and giants. Since the γ-ray emission is thought to be highly sensitive to the jet viewing angle, such an enlarged sample of γ-ray detected misaligned radio sources will permit us to explore the origin of high-energy emission in relativistic jets and radio lobes and study AGN unification, in general.

Unified Astronomy Thesaurus concepts: BL Lacertae objects (158); Fanaroff-Riley radio galaxies (526); Gamma-ray astronomy (628); Relativistic jets (1390); Radio jets (1347)

1. Introduction

Radio galaxies are thought to be the misaligned version of beamed active galactic nuclei (AGN), namely the blazars, which consist of flat-spectrum core-dominated quasars and BL Lac objects (see C. M. Urry & P. Padovani 1995, for a review). A radio-loud quasar is considered to be a misaligned jetted AGN if the viewing angle of the jet θ_v is $>1/\Gamma$, where Γ is the bulk Lorentz factor of the jet. Because of the large viewing angle, the radiation emitted from either a radio galaxy or a misaligned quasar is less boosted compared to that observed from blazars. These sources at large viewing angles are mostly identified at radio wavelengths where the radiation is dominated primarily by the mildly relativistic outflows from the extended jets and hotspots or nearly isotropic emission originating from the radio lobes (see D. J. Saikia 2022, for a recent review). Radio galaxies and quasars have been classified as Fanaroff–Riley Type I (FR I) and FR II sources based on their extended radio structure, with the former being less luminous with an edge-darkened structure and reasonably symmetric large-scale radio jets. The FR II sources are edge-brightened, usually with prominent hotspots along with asymmetric large-scale jets, and are found to be more luminous (B. L. Fanaroff & J. M. Riley 1974). However, recent low-frequency observations taken with the Low-Frequency Array (LOFAR) have revealed that the radio luminosity may not reliably predict the morphology and classification of a radio galaxy (B. Mingo et al. 2019). Furthermore, hybrid

morphology radio sources, i.e., those exhibiting an FR II radio structure on one side and an FR I jet on the other, have also been reported (see D. J. Saikia et al. 1996; W. P. J. Gopal-Krishna 2000). More recently, there have been suggestions that the hybrid morphology sources are the result of orientation and are intrinsically FR II radio sources (J. J. Harwood et al. 2020). The optical spectroscopic observations of radio galaxies have also led to their classification into high-excitation radio galaxies (HERGs) and low-excitation radio galaxies (LERGs), with the former having radiatively efficient accretion (see P. N. Best & T. M. Heckman 2012; T. M. Heckman & P. N. Best 2014). However, recent LOFAR observations have indicated a complex relationship between FR class and accretion mode in radio sources (B. Mingo et al. 2019, 2022).

In the high-energy γ-ray band (0.1–300 GeV), the number of known radio galaxies is small ($\sim$50) compared to blazars which dominate the extragalactic γ-ray sky (e.g., A. A. Abdo et al. 2010b; P. Grandi et al. 2012; G. Chiaro et al. 2020; M. Ajello et al. 2022). This can be understood due to the relatively large viewing angle causing de-boosting of the emitted radiation from the jet. Therefore, the detection of γ-ray emission from radio galaxies may be indicative of a different emission region location and/or physical processes. Indeed, the extended γ-ray emission originating from the lobes of the radio galaxy Centaurus A has been observed (A. A. Abdo et al. 2010a). Y. Fukazawa et al. (2022) carried out a systematic study of γ-ray detected radio galaxies present in the second data release of the fourth Fermi-Large Area Telescope (LAT) γ-ray source catalog and determined that these objects may contribute up to $\sim$10% of the extragalactic γ-ray background. The γ-ray emission in these objects has been typically explained with synchrotron self-Compton radiative models

(e.g., Y. Fukazawa et al. 2018). However, several complex models, e.g., spine-sheath structured jet, have also been put forward to explain the γ-ray observations of radio galaxies (D. Giannios et al. 2010; G. Migliori et al. 2011).

The identification of radio galaxies in the γ-ray band has primarily been done by crossmatching the list of known radio galaxies with Fermi-LAT catalogs (see A. A. Abdo et al. 2010b). A majority of these radio galaxies were found in dedicated observations and/or previous generation low-resolution surveys, e.g., NRAO VLA Sky Survey, that permitted us to identify mainly the large-scale radio structures extending up to Mpc scales (e.g., J. J. Condon & J. J. Broderick 1988; C. H. Ishwara-Chandra & D. J. Saikia 1999; P. Dabhade et al. 2023). With the advent of sensitive, wide-field, high-resolution radio surveys, e.g., the Very Large Array Sky Survey (VLASS), it is now possible to identify radio galaxies with comparatively smaller linear sizes. Indeed, several γ-ray sources that were not known as misaligned AGN have recently been found to exhibit radio structures typical of FR I/II radio galaxies (see G. Bruni et al. 2022; V. S. Paliya et al. 2023). Additionally, a new population of γ-ray emitting FR 0 radio galaxies has also emerged in the γ-ray sky (e.g., P. Grandi et al. 2016; V. S. Paliya 2021; M. Pannikkote et al. 2023). These observations suggest that there could be many more high-energy emitting misaligned AGN than currently known. They may have remained unresolved/partially resolved in previous surveys, possibly due to poorer spatial resolution.

Enlarging the γ-ray emitting radio galaxy population is crucial for sample studies, improving source classification of the Fermi-LAT catalogs, and constraining the contribution of radio galaxies to the extragalactic γ-ray background (see M. Di Mauro et al. 2014; F. W. Stecker et al. 2019; Y. Fukazawa et al. 2022). Furthermore, a larger sample also permits understanding the radiative processes responsible for the observed high-energy emission and studying the surrounding environment in which they grow and launch relativistic jets (e.g., Y. Chen et al. 2023). With these objectives in mind, we utilized the latest multi-frequency radio surveys to study the morphological properties of all known γ-ray sources. Here, we report those γ-ray sources that exhibit extended radio morphologies in at least one of the considered radio surveys. We also used the optical spectroscopic observations, when available, to identify γ-ray detected misaligned AGN with high confidence. Section 2 briefly describes the sample selection and multiwavelength radio catalogs whose data were used in this work. The results are presented and discussed in Sections 3 and 4, respectively. We summarize our findings in Section 5. A flat cosmology with $H_0 = 70 \, \mathrm{km \, s^{-1} \, Mpc^{-1}}$ and $\Omega_M = 0.3$ was adopted.

2. Sample Selection and Multiwavelength Catalog

2.1. The Sample

The fourth data release of the fourth Fermi-LAT γ-ray source catalog (4FGL-DR4) contains 7194 astrophysical objects significantly detected at γ-ray energies (S. Abdollahi et al. 2022; J. Ballet et al. 2023). Among them, we considered those 4069 γ-ray sources whose multiwavelength counterparts have been reported to be AGN, e.g., blazars and radio galaxies. The radio morphologies of these objects were inspected using the data provided by the multi-frequency radio surveys described below. The counterpart coordinates of γ-ray sources given in the 4FGL-DR4 catalog were used for this purpose.

There are 2430 unidentified γ-ray sources (unIDs) present in the 4FGL-DR4 catalog for which multiwavelength counterparts remained unidentified. To determine the potential counterparts, we have utilized several multiwavelength catalogs, e.g., the Chandra Source Catalog, and considered only those sources located within the γ-ray uncertainty region of unID that have been detected in the X-ray, radio, and optical/infrared (IR) bands. The details of the adopted steps are provided in Appendix A. We considered these 476 potential counterparts and studied their radio morphologies to identify γ-ray emitting radio galaxies among them.

2.2. Radio Catalogs

We used the following radio surveys to study the morphologies of the sources under consideration:

VLASS. It is an ongoing radio survey at 2−4 GHz covering the whole sky visible at VLA ($\delta > -40°$). The angular resolution is ∼2″.5 and the rms sensitivity for a single epoch is $120 \, \mu\mathrm{Jy \, beam^{-1}}$. The observations are being carried out in three epochs to study transient astrophysical objects. Further details about the survey can be found in M. Lacy et al. (2020). We downloaded the $5 \times 5 \, \mathrm{arcmin^2}$ cutout images of 3676 sources. The images were downloaded from the Canadian Initiative for Radio Astronomy Data Analysis website.[4]

Faint Images of the Radio Sky at Twenty Centimeters (FIRST). It is the previous generation survey conducted at 1.4 GHz with a typical rms sensitivity of $0.15 \, \mathrm{mJy \, beam^{-1}}$, and a resolution of ∼5″ (D. J. Helfand et al. 2015). We downloaded the $5 \times 5 \, \mathrm{arcmin^2}$ cutout images of 1300 sources from the FIRST cutout server.[5]

LOFAR. The second data release of the LOFAR Two-meter Sky Survey (LOTSS-DR2) covers areas of 4178 and 1457 $\mathrm{deg^2}$ centered at ($12^\mathrm{h} \, 45^\mathrm{m}, +44° \, 30'$) and ($1^\mathrm{h} \, 00^\mathrm{m} +28° \, 00'$). In the 120−168 MHz frequency band, a resolution of 6″ and a median rms sensitivity of $83 \, \mu\mathrm{Jy \, beam^{-1}}$ have been achieved (T. W. Shimwell et al. 2022). We retrieved $30 \times 30 \, \mathrm{arcmin^2}$ cutout images of 770 objects from the LOFAR data server.[6]

Rapid ASKAP Continuum Survey (RACS). This ongoing survey utilizes the full 36-dish Australian Square Kilometre Array Pathfinder (ASKAP) telescope. A new catalog of sources detected at 1367.5 MHz (RACS-mid) was released, covering the sky south of decl. +49° (S. W. Duchesne et al. 2024). The median angular resolution of the survey is 11″.2 × 9″.3 though it varied to maximize sky coverage and sensitivity across the covered area of ∼36200 $\mathrm{deg^2}$. We extracted $30 \times 30 \, \mathrm{arcmin^2}$ cutout images of 1267 objects from this catalog.[7]

The choice of different cutout sizes was based on the resolution and the operating frequency of the adopted surveys. For example, VLASS has the highest resolution among all the surveys; hence, the large-scale diffuse emission is expected to be completely resolved out, thus undetected. Also, the largest angular size of the known double-lobed radio sources in the VLASS is only ∼3′ (Y. A. Gordon et al. 2023). Therefore, small-sized cutouts were downloaded. On the other hand, low-frequency surveys, such as RACS and LOFAR, are expected to detect diffuse emission mainly originating from the large-scale lobes, so larger cutouts were retrieved from their databases.

---

[4] http://cutouts.cirada.ca
[5] https://third.ucllnl.org/cgi-bin/firstcutout
[6] https://lofar-surveys.org/dr2_release.html
[7] https://research.csiro.au/casda/

3. Results

We retrieved and visually inspected the radio cutout images from the abovementioned surveys. We started with the VLASS data and segregated the sources into two lists: one for sources whose VLASS images revealed double-lobed morphology and the other for remaining objects. The radio morphologies of sources present in the second list were then inspected using the FIRST images when available, and the source lists were updated. This procedure was then repeated for the LOFAR and RACS surveys, respectively.

Since the VLASS quick-look images can be affected by artifacts, it is possible that an extended radio structure may not be clearly visible due to image distortion and/or the presence of bright streaks. Alternatively, a false detection can appear like an extended radio jet.[8] Also, this high-frequency, high-resolution survey may resolve out diffuse extended emission. To take into account these issues and for consistency check, the radio images taken in other surveys, when available, were inspected for all γ-ray sources whose radio morphology was found to exhibit double-lobed structure in at least one of the considered surveys. Moreover, since VLASS quick-look images are available for several epochs, we ensured that an extended radio structure is detected in all of them.

In addition to the double-lobed morphology, which can be affected by projection effects, we adopted the following three techniques to identify the best γ-ray emitting misaligned AGN candidates: (i) visual inspection of the optical spectrum, (ii) calculation of the core dominance, and (iii) overall radio spectral index.

According to the AGN unification scheme, the strength of the broad emission lines decreases as the viewing angle increases and the radiation from the host galaxy stellar population starts dominating. Therefore, an optical spectrum consisting primarily of narrow emission lines and/or galaxy spectral features, e.g., Ca II H/K break, indicates a large viewing angle. With this idea in mind, we also collected the available optical spectra from the literature for all sources exhibiting double-lobed radio morphologies.

The core dominance is considered a good proxy for the orientation of the beamed emission since the core emission is Doppler boosted, whereas the lobe emission can be assumed reasonably isotropic (see R. Morganti et al. 1997). This parameter was derived from the following relation:

$$C_{\rm D} = \log\left(\frac{F_{\rm core}}{F_{\rm ext}}(1 + z)^{\alpha_{\rm core} - \alpha_{\rm ext}}\right). \qquad (1)$$

The parameters $\alpha_{\rm core}$ and $\alpha_{\rm ext}$ are spectral indices ($F(\nu) \propto \nu^\alpha$) of the core and extended emission, respectively, and were taken as $\alpha_{\rm core} = 0$ and $\alpha_{\rm ext} = -0.8$. The parameters $F_{\rm core}$ and $F_{\rm ext}$ ($= F_{\rm total} - F_{\rm core}$) refer to the core and extended flux densities, respectively, and were estimated at rest-frame 3 GHz, assuming the spectral indices mentioned above. For sources without redshift information, we derived the core dominance as $C_{\rm D} = \log\frac{F_{\rm core}}{F_{\rm ext}}$, i.e., at the observed 3 GHz frequency. For blazars, $C_{\rm D}$ is reported to be large (>1; M. J. Marcha et al. 2001; Y. Y. Chen et al. 2015). On the other hand, using Very Long Baseline Interferometry observations, R. Angioni et al. (2019) found the core dominance of the Fermi-LAT detected radio galaxies to be <1.

The overall radio spectral shape of an AGN can also give hints about the jet misalignment. Sources viewed close to the line of sight, i.e., blazars, usually exhibit a flat radio spectrum throughout MHz-to-GHz frequencies (spectral index $\alpha > -0.5$, Ž. Ivezić et al. 2002; S. E. Healey et al. 2007; F. Massaro et al. 2014). On the other hand, radio galaxies often exhibit steep radio spectra. Depending on the degree of core dominance at different frequencies, sources may also have a steep spectrum at low frequencies due to the extended emission and a flat spectrum at high frequencies where the core dominates. We used the SPECFIND (v3.0) catalog to determine the radio spectral indices of the sources under consideration (Y. Stein et al. 2021). For eight objects not present in this catalog, we determined their spectral indices by taking the integrated flux densities from the NRAO VLA Sky Survey (1.4 GHz), TIFR GMRT Sky Survey (150 MHz), LOFAR (144 MHz), Galactic and Extragalactic All-sky MWA survey (200 MHz), and the Sydney University Molonglo Sky Survey (843 MHz), depending on the presence of objects in the footprints of these surveys.

The visual inspection of all cutout images led to the identification of 219 sources where double-lobed radio emission was noticed in at least one of the abovementioned radio surveys. We then devised a strategy that a source is considered as a promising γ-ray emitting misaligned AGN only if at least two of the adopted three observables, i.e., optical spectrum, core dominance, and radio spectral index, resemble known misaligned radio sources. This exercise led to the final sample of 149 γ-ray emitting objects.

We were able to retrieve the optical spectra of 103 sources, including two of them from our own observations taken at Telescopio Nazionale Galileo (N. Álvarez Crespo et al., 2024, in preparation). The remaining 46 objects either do not have optical spectroscopic observations or the spectral plots are not published. There are 86 sources whose optical spectra are dominated by host galaxy absorption features, whereas 17 sources exhibit broad emission lines in their optical spectra. Considering the radio spectra, 116 sources have $\alpha < -0.5$, i.e., a steep radio spectrum. Among the remaining 33 sources, 8 have a radio spectral index close to the steep/flat spectral shape boundary, i.e., $-0.5 < \alpha < -0.45$. The logarithmic core dominance is found to be less than 0.5 for 147, and only two sources have core-dominated emissions. Among these 147 objects, 106 have lobe-dominated emission, i.e., $C_{\rm D} < 0$. Finally, we also classified sources as FR I and IIs based on their observed morphologies. There are 64 and 71 objects exhibiting FR I and II radio structures, respectively. We have also found 14 γ-ray emitters that show a hybrid radio morphology, i.e., FR I type diffuse emission on one side and edge-brightened FR II lobes on the opposite side of the core. We show one of their radio images and optical spectrum in Figure 1 and list all sources in Table 1. The contours from the radio survey data in which the double-lobed morphology was the best seen were overplotted on the Panoramic Survey Telescope and Rapid Response System (PanSTARRS; K. C. Chambers et al. 2016) or Dark Energy Survey (T. M. C. Abbott et al. 2021) i-band images. For completeness, the radio contours using other survey data, when available, were also plotted. The plots for the remaining objects can be found on Zenodo, available at doi:10.5281/zenodo.13908693.

We estimated the total flux density using the survey data with the largest beam size, i.e., lowest resolution, to ensure that no diffuse extended flux density is missed out. The core flux
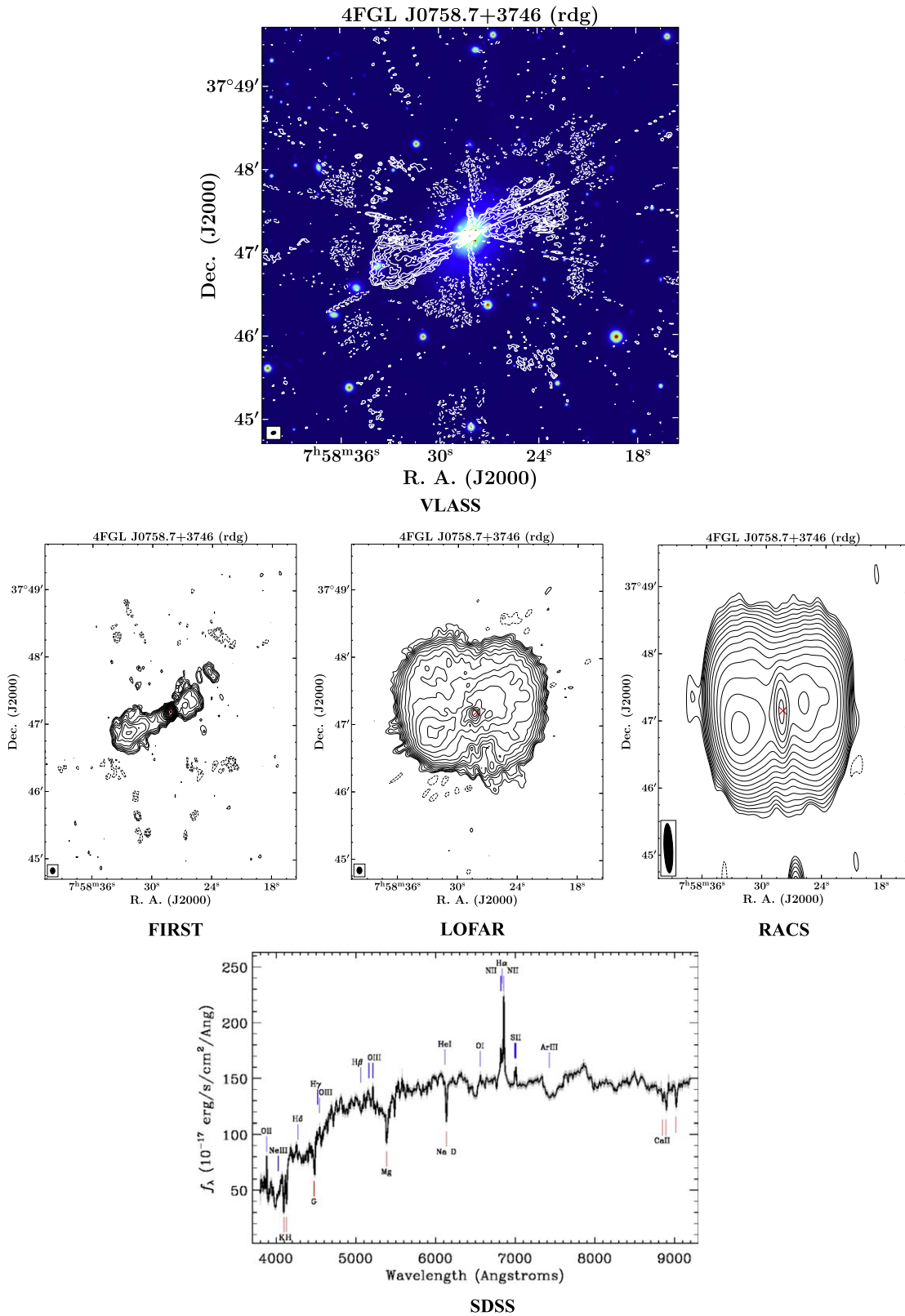
---

[8] https://science.nrao.edu/vlass/data-access/vlass-epoch-1-quick-look-users-guide

Figure 1. The VLASS contours overplotted on PanSTARRS *i*-band images of one of the γ-ray emitting AGN exhibiting double-lobed radio structure (top panel). Along with the 4FGL name, we also mention the classification reported in the 4FGL-DR4 catalog (S. Abdollahi et al. 2022). The radio morphologies observed by other surveys, when available, are plotted in the middle panel. In all plots, the contour levels start at $3 \times \mathrm{rms} \times (-2, -\sqrt{2}, -1, 1)$ and increase in multiple of $\sqrt{2}$. The bottom panel shows the optical spectrum of the source when available. By default, the north is up and east to the left. For DECAM optical images, we have added a compass to guide the eye. The references for the shown optical spectra are provided in Table 1. The complete figure set is available on ZENODO (doi:10.5281/zenodo.13908693).

Table 1
The List of γ-Ray Emitting Misaligned Jetted AGN

4FGL Name [1]	R.A. [2]	Decl. [3]	z [4]	Γ_γ [5]	α [6]	LAS [7]	F_{core} [8]	F_{total} [9]	C_D [10]	Morph. [11]	Survey 12	Reference 13
J0001.4−0010	0.33954	−0.19441	0.461	2.11 ± 0.18	−0.57	70.5	32.29 ± 0.26	113.49 ± 0.78	0.006	FR I	R V R	A20
J0009.7−3217	2.39816	−32.27691	0.025	2.26 ± 0.10	−0.45	211.2	210.77 ± 0.46	445.29 ± 1.66	0.237	FR I	R V R	J09
J0013.6+4051	3.37970	40.86031	0.255	2.28 ± 0.14	−0.53	34.1	539.50 ± 0.61	1600.79 ± 2.44	0.060	FR I–II	V V R	S93
J0014.2+0854	3.58224	8.90056	0.163	2.50 ± 0.12	−0.60	118.9	74.54 ± 0.22	362.44 ± 1.15	−0.260	FR I	R V R	A20
J0018.8+2611	4.91575	26.04788	0.280	2.81 ± 0.10	−0.52	54.6	272.48 ± 0.63	756.53 ± 1.21	0.111	FR II	V V R	Z12
J0037.9+2612	9.32983	26.22008	0.148	2.45 ± 0.12	−0.37	411.1	79.01 ± 0.29	556.61 ± 2.22	0.322	FR I	L V L	A20
J0038.7−0204	9.58553	−2.12792	0.220	2.76 ± 0.11	−0.74	19.9	509.48 ± 0.31	6297.47 ± 4.00	−0.711	FR II	V V R	A20
J0044.9+4553	11.25014	45.92090	0.179	2.49 ± 0.13	−0.59	14.0	190.74 ± 0.38	377.22 ± 0.74	0.342	FR II	V V R	Z12
J0057.7+3023	14.45368	30.35244	0.016	2.39 ± 0.09	−0.30	3410.1	528.56 ± 0.63	10495.50 ± 10.52	−0.215	FR I	L V L	J00
J0112.8−0253	18.20390	−2.91769	0.188	2.06 ± 0.18	−0.73	86.8	14.54 ± 0.36	102.24 ± 0.98	−0.445	FR I	R V R	A20
J0119.6+4158	20.01148	42.00386	0.109	2.37 ± 0.15	−0.60	117.71	29.25 ± 0.26	246.29 ± 1.20	−0.560	FR I	L V R	D20
J0126.5−1553	21.78538	−15.93171	0.988	2.54 ± 0.17	−0.58	93.7	26.66 ± 0.25	107.36 ± 0.78	0.033	FR II	R V R	F22
J0153.4+7114	28.35771	71.25179	0.022	1.90 ± 0.11	−0.43	118.4	367.60 ± 0.46	543.03 ± 2.54	0.329	FR I	V V V	M96
J0204.3+2417	31.08977	24.29741	0.210	1.95 ± 0.15	−0.61	68.0	81.46 ± 0.38	213.27 ± 0.78	0.132	FR I	L V R	D20
J0222.7+5016	35.76560	50.27069	−999	2.17 ± 0.12	−0.80	17.6	5.41 ± 0.32	25.17 ± 0.75	−0.563	FR II	V V V	...
J0237.7+0206	39.42408	1.97531	0.021	2.14 ± 0.14	0.00	487.8	23.07 ± 0.24	164.32 ± 2.06	−0.505	FR I	R V R	Z12
J0305.1−1608	46.31278	−16.13796	0.311	1.77 ± 0.09	−0.77	24.9	29.62 ± 0.31	902.12 ± 1.55	−1.100	FR II	V V R	P17
J0308.4+0407	47.10924	4.11091	0.029	2.01 ± 0.05	−0.59	208.2	873.09 ± 0.85	7510.69 ± 4.33	−0.596	FR I	R V R	B09
J0309.9−6941	47.20726	−69.77450	−999	2.46 ± 0.15	−0.42	18.2	7.03 ± 0.09	31.97 ± 0.28	−0.275	FR II	R R R	...
J0309.4−4000	47.30425	−40.03077	0.193	2.01 ± 0.13	−0.77	145.0	124.20 ± 0.31	352.28 ± 1.57	0.072	FR I	R R R	P21
J0316.8+4120	49.17907	41.32489	0.018	1.88 ± 0.12	−0.22	370.0	125.51 ± 1.19	627.98 ± 2.80	−0.321	FR I	R V R	A20
J0320.6+2728	50.16735	27.46344	0.060	2.44 ± 0.15	−0.34	473.0	8.40 ± 0.25	396.69 ± 1.81	−1.370	FR I	R V R	H12
J0321.3−1612	50.29293	−16.21122	0.459	2.10 ± 0.18	−0.70	87.9	1.60 ± 0.39	114.52 ± 0.93	−1.443	FR I	R V R	F22
J0322.6−3712e	50.67412	−37.20820	0.005	2.07 ± 0.05	−0.77	106.8	63.07 ± 0.41	348.52 ± 1.95	−0.379	FR I	R V R	L17
J0334.3+3920	53.57672	39.35677	0.020	1.82 ± 0.10	−0.55	180.6	276.33 ± 0.42	988.40 ± 1.80	−0.129	FR I	R V R	Z12
J0418.2+3807	64.58865	38.02661	0.048	2.76 ± 0.05	−0.74	204.3	1456.67 ± 1.71	14984.60 ± 15.69	−0.677	FR II	R V R	B09
J0431.0+3529c	67.63673	35.44046	−999	2.64 ± 0.14	−0.73	56.5	1.91 ± 0.26	66.82 ± 0.87	−1.256	FR II	V V R	...
J0515.5−0125	78.90076	−1.40747	1.160	2.11 ± 0.09	−0.96	10.2	3.60 ± 0.20	100.17 ± 0.55	−0.886	FR II	V V R	F22
J0519.6+2744	79.88762	27.73452	0.068	2.02 ± 0.16	−0.54	156.6	133.71 ± 0.35	1697.87 ± 2.54	−0.770	FR I	R V R	B14
J0519.6−4544	79.95716	−45.77886	0.035	2.57 ± 0.12	−1.09	496.8	1106.36 ± 1.79	64940.10 ± 27.13	−1.474	FR II	R R R	B02
J0522.9−3628	80.74160	−36.45856	0.056	2.45 ± 0.01	−0.63	38.9	2488.72 ± 3.95	17839.80 ± 16.31	−0.496	FR I–II	V V R	S06
J0525.6−2008	81.36683	−20.18011	0.092	2.22 ± 0.11	−0.19	511.8	112.27 ± 0.35	250.24 ± 1.67	0.216	FR I	R V R	Pa21
J0539.2−6333	84.73453	−63.54380	−999	1.96 ± 0.14	−0.68	21.6	9.69 ± 0.16	72.23 ± 0.62	−0.535	FR II	R R R	...
J0550.5−3216	87.66904	−32.27124	0.069	1.83 ± 0.07	−0.44	133.6	96.19 ± 0.50	472.95 ± 1.50	−0.295	FR I	R V R	F76
J0551.8−3517	87.92625	−35.25921	0.332	2.10 ± 0.17	−0.89	110.3	28.48 ± 0.35	88.06 ± 0.83	0.054	FR II	R V R	F22
J0627.0+2623	96.72875	26.38883	0.157	1.60 ± 0.19	−0.57	22.2	129.23 ± 0.32	1413.70 ± 1.57	−0.672	FR I–II	V V R	B14
J0627.0−3529	96.77804	−35.48758	0.054	1.91 ± 0.03	−0.65	214.0	1417.74 ± 0.42	4597.49 ± 3.95	−0.057	FR I	R V R	J09
J0643.4−3314	100.89416	−33.24182	−999	2.44 ± 0.16	−0.66	14.8	58.01 ± 0.23	218.08 ± 0.51	−0.166	FR II	V V R	...
J0656.3+4235	104.04442	42.61743	0.059	1.97 ± 0.11	−0.50	54.9	190.05 ± 0.22	940.97 ± 0.74	−0.302	FR I	V V R	L98
J0708.9+4839	107.28335	48.61548	0.019	1.72 ± 0.14	−0.66	443.2	140.44 ± 0.20	715.09 ± 2.56	−0.330	FR I	R V R	Z12
J0715.7−1128	108.72867	−11.56226	−999	2.61 ± 0.09	−0.68	43.9	9.83 ± 0.28	305.80 ± 1.18	−1.204	FR II	V V R	...
J0733.0+4915	113.24325	49.28264	0.668	2.23 ± 0.19	−0.58	16.2	41.20 ± 0.19	122.11 ± 1.21	0.160	FR I	V V R	**
J0758.7+3746	119.61711	37.78661	0.042	2.26 ± 0.13	−0.59	187.1	189.81 ± 0.29	2687.06 ± 2.80	−0.830	FR I	R V R	A20
J0828.6−0747	127.22741	−7.81488	0.415	2.45 ± 0.10	−0.75	20.6	18.25 ± 0.22	278.75 ± 0.81	−0.759	FR I–II	V V R	F22
J0829.0+1755	127.27011	17.90440	0.089	2.15 ± 0.08	−0.48	85.8	132.20 ± 0.22	298.00 ± 1.24	0.206	FR I–II	R V R	A20
J0840.8+1317	130.19828	13.20654	0.681	2.48 ± 0.10	−0.72	10.0	825.86 ± 1.25	2947.94 ± 2.71	0.045	FR II	V V R	A20
J0850.4−2558	132.38361	−26.03034	−999	2.44 ± 0.21	−0.96	66.2	2.67 ± 0.27	25.21 ± 0.62	−0.652	FR II	V V R	...

Table 1
(Continued)

4FGL Name [1]	R.A. [2]	Decl. [3]	z [4]	Γ_γ [5]	α [6]	LAS [7]	$F_{\rm core}$ [8]	$F_{\rm total}$ [9]	$C_{\rm D}$ [10]	Morph. [11]	Survey 12	Reference 13
J0858.1+1405	134.67269	14.16243	1.048	2.46 ± 0.11	−0.84	10.7	354.83 ± 0.57	2438.45 ± 0.69	−0.245	FR II	V V R	A20
J0904.0+2724	135.88755	27.32437	1.723	2.75 ± 0.07	−0.83	17.4	80.71 ± 0.29	207.34 ± 0.78	0.427	FR I−II	V V R	A20
J0903.5+4057	135.92993	40.91753	0.890	2.03 ± 0.19	−0.91	95.0	2.96 ± 0.29	9.15 ± 0.45	0.176	FR II	L V R	A20
J0912.9−2102	138.25091	−21.05583	0.198	1.82 ± 0.04	−0.26	86.7	166.88 ± 0.49	368.61 ± 0.96	0.255	FR II	R V R	J09
J0913.9+1732	138.49092	17.57008	−999	2.34 ± 0.20	−0.78	4.8	32.88 ± 0.25	101.49 ± 0.41	−0.045	FR II	V V R	...
J0920.2−3835	140.05929	−38.58072	0.145	2.02 ± 0.17	−0.95	112.6	91.03 ± 0.29	703.63 ± 2.40	−0.506	FR I−II	R V R	B14
J0929.3−2414	142.36767	−24.27579	0.208	2.12 ± 0.14	−0.74	92.8	37.39 ± 0.29	240.52 ± 1.43	−0.394	FR I−II	R V R	P21
J0948.0−3859	147.14675	−38.98312	−999	2.64 ± 0.14	−0.85	132.3	4.53 ± 0.30	86.99 ± 1.01	−0.985	FR I	R V R	...
J0957.3−3851	149.64464	−38.85703	−999	2.90 ± 0.15	−0.78	21.6	72.39 ± 0.31	322.09 ± 0.68	−0.263	FR II	V V R	...
J0958.3−2656	149.60245	−26.92666	0.009	2.13 ± 0.14	−0.46	175.4	179.47 ± 0.36	325.31 ± 0.92	0.368	FR I	R V R	O08
J1008.2−1000	152.00977	−9.98878	1.688	3.02 ± 0.15	−1.01	14.6	35.19 ± 0.35	627.34 ± 0.60	−0.608	FR II	V V R	K18
J1008.0+0028	152.04765	0.49998	0.097	2.15 ± 0.07	−0.49	48.5	74.97 ± 0.27	472.82 ± 1.65	−0.418	FR I−II	V V R	P21
J1106.2−1048	166.52338	−10.81481	0.242	2.23 ± 0.13	−0.67	27.1	34.73 ± 0.29	266.35 ± 0.77	−0.474	FR II	V V R	F22
J1116.6+2915	169.14424	29.25475	0.046	1.68 ± 0.26	−0.58	63.1	38.89 ± 0.54	1891.66 ± 2.14	−1.387	FR II	V V R	A20
J1121.3−0011	170.33092	−0.22134	0.099	1.92 ± 0.14	−0.52	145.4	116.22 ± 0.33	641.30 ± 1.74	−0.347	FR I	R V R	G23
J1139.6+1149	175.11538	12.05206	0.081	2.78 ± 0.15	−0.70	174.4	32.71 ± 0.27	1462.91 ± 2.23	−1.339	FR I	R V R	A20
J1144.9+1937	176.27087	19.60631	0.021	2.01 ± 0.08	−0.73	616.9	360.47 ± 0.39	5513.38 ± 8.11	−0.873	FR I	R V R	A20
J1146.4−3327	176.61854	−33.47850	0.294	2.43 ± 0.13	−0.66	25.6	223.32 ± 0.33	1591.96 ± 1.60	−0.423	FR II	V V R	M11
J1202.4+4442	180.53609	44.73957	0.297	2.47 ± 0.18	−0.52	178.1	45.86 ± 0.37	104.86 ± 0.99	0.256	FR I	L V R	A20
J1205.7−2635	181.38838	−26.56790	0.789	2.53 ± 0.05	−0.55	15.4	358.26 ± 0.66	1535.06 ± 1.23	−0.040	FR II	V V R	W83
J1216.1+0930	184.02587	9.48600	0.093	2.05 ± 0.07	−0.10	285.6	92.65 ± 0.34	183.94 ± 1.58	0.312	FR I	R V R	A20
J1219.6+0550	184.84674	5.82491	0.007	2.17 ± 0.13	−0.47	534.9	296.56 ± 0.40	17724.20 ± 10.32	−1.492	FR I	R V R	G04
J1226.9+6405	186.59378	64.10612	0.110	2.67 ± 0.14	−0.18	411.5	43.66 ± 0.25	608.56 ± 1.72	−0.021	FR I	L V L	A20
J1227.8+6053	186.93893	60.87166	0.634	2.16 ± 0.21	−0.79	31.5	22.23 ± 0.28	522.17 ± 0.42	−0.126	FR I−II	L V L	A20
J1230.8+1223	187.70593	12.39112	0.004	2.06 ± 0.03	−0.68	658.7	2821.31 ± 6.96	158617.00 ± 237.79	−1.466	FR I	R V R	B09
J1230.9+3711	187.85039	37.18392	0.218	2.43 ± 0.24	−1.00	186.9	16.61 ± 0.22	186.42 ± 1.42	−0.666	FR I−II	L V R	A20
J1233.6+5027	188.45527	50.43965	0.206	2.20 ± 0.08	−0.54	18.5	71.49 ± 0.24	1085.35 ± 0.81	−0.031	FR II	V V L	A20
J1236.9−7232	189.29889	−72.59203	0.023	2.43 ± 0.11	−0.88	789.2	308.54 ± 0.46	970.18 ± 3.89	−0.048	FR I	R R R	L11
J1256.9+2736	194.35147	27.49790	0.024	2.68 ± 0.14	−0.82	146.1	3.53 ± 0.20	77.66 ± 0.68	−1.039	FR I	R V R	A20
J1258.7+5143	194.60580	51.70725	0.463	2.31 ± 0.14	−0.56	47.4	3.72 ± 0.28	263.07 ± 0.40	−0.656	FR II	V V L	Z12
J1302.7+4750	195.70292	47.91963	0.140	2.56 ± 0.26	−0.45	158.4	4.31 ± 0.30	204.52 ± 0.55	−0.566	FR I	L V L	A20
J1305.9+3858	196.38000	38.92250	0.376	2.20 ± 0.15	−0.65	120.6	10.89 ± 0.24	40.49 ± 0.53	−0.049	FR I	L V R	A20
J1306.3+1113	196.58019	11.22772	0.085	1.87 ± 0.14	−0.73	112.4	93.98 ± 0.26	417.11 ± 1.55	−0.233	FR I	R V R	A20
J1306.7−2148	196.6752	−21.79749	0.126	2.17 ± 0.07	−0.48	285.0	81.99 ± 0.32	578.07 ± 2.30	−0.466	FR I	R V R	G83
J1310.6+2449	197.66051	24.80636	0.226	2.00 ± 0.09	−0.70	63.6	38.58 ± 0.27	116.63 ± 0.66	0.040	FR II	L V R	D20
J1311.8+2057	197.93103	20.86903	0.724	2.84 ± 0.76	−0.76	25.1	6.95 ± 0.36	157.35 ± 0.87	−0.871	FR II	V V R	F22
J1325.5−4300	201.36508	−43.01911	0.001	2.57 ± 0.02	−0.65	901.2	4645.56 ± 2.87	246883.00 ± 56.38	−1.442	FR I	R R R	L11
J1326.2+4115	201.49559	41.25008	0.309	2.45 ± 0.10	−0.46	127.3	61.15 ± 0.20	141.37 ± 0.80	0.251	FR I	L V R	A20
J1327.0+3154	201.88215	31.85755	0.239	2.20 ± 0.23	−0.56	21.4	172.55 ± 0.72	1393.10 ± 2.32	−0.500	FR II	V V R	A20
J1334.5+5634	203.65622	56.52996	0.342	2.35 ± 0.16	−0.55	27.0	74.67 ± 0.23	844.24 ± 0.49	0.144	FR II	V V L	A20
J1340.1+3857	204.70827	38.85298	0.246	2.54 ± 0.12	−0.96	12.7	76.32 ± 0.26	3549.63 ± 1.35	−1.307	FR II	V V R	B09
J1341.2+3958	205.27127	39.99594	0.172	1.79 ± 0.08	−0.56	123.5	31.46 ± 0.36	87.24 ± 0.59	0.081	FR I	L V R	A20
J1342.7+0505	205.68176	5.07561	0.136	2.20 ± 0.09	−0.62	83.8	379.75 ± 0.38	1771.29 ± 2.37	−0.245	FR I	R V R	A20
J1344.4−3656	206.09910	−36.94133	−999	2.16 ± 0.09	−0.70	15.2	55.63 ± 0.35	491.88 ± 0.94	−0.620	FR II	V V R	...
J1346.5+5330	206.43898	53.54785	0.135	2.68 ± 0.08	−0.56	187.4	119.69 ± 0.44	1629.20 ± 1.63	−0.002	FR I	L V L	A20
J1346.3−6026	206.70458	−60.40833	0.012	2.39 ± 0.04	−2.14	985.5	4455.95 ± 2.78	20844.80 ± 39.37	−0.286	FR I−II	R R R	W89
J1347.9−0618	207.02731	−6.35807	−999	2.14 ± 0.17	−0.77	27.6	14.76 ± 0.29	248.29 ± 0.95	−0.924	FR II	V V R	...

Table 1
(Continued)

4FGL Name [1]	R.A. [2]	Decl. [3]	z [4]	Γ_γ [5]	α [6]	LAS [7]	F_{core} [8]	F_{total} [9]	C_D [10]	Morph. [11]	Survey 12	Reference 13
J1352.6+3133	208.07420	31.44628	0.045	2.64 ± 0.14	−0.62	217.9	1994.23 ± 1.74	4762.99 ± 4.73	0.148	FR II	L V R	A20
J1354.8−1041	208.69382	−10.68407	0.330	2.47 ± 0.04	−0.35	29.6	375.03 ± 0.35	709.36 ± 1.05	0.424	FR II	V V R	W83
J1402.6+1600	210.68547	15.99907	0.244	2.19 ± 0.12	−0.54	18.7	277.80 ± 0.46	884.87 ± 0.85	0.011	FR II	V V R	A20
J1413.1−6519	213.29123	−65.33887	0.001	2.24 ± 0.10	−0.63	306.3	582.91 ± 0.31	1335.45 ± 2.29	0.164	FR I	R R R	K04
J1435.5+2021	218.84141	20.35496	0.748	2.20 ± 0.09	−0.71	19.9	56.43 ± 0.28	353.93 ± 0.62	−0.253	FR II	V V R	A20
J1443.1+5201	220.76150	52.02702	0.141	2.11 ± 0.11	−0.73	33.3	207.54 ± 0.58	14286.90 ± 8.54	−0.731	FR II	V V L	A20
J1453.0−1318	223.24231	−13.32303	−999	2.43 ± 0.13	−0.66	12.1	281.46 ± 0.37	766.56 ± 0.96	0.038	FR II	V V R	...
J1455.4−3654	223.79009	−36.91874	0.094	2.43 ± 0.11	−0.79	234.5	209.22 ± 0.53	1145.48 ± 2.72	−0.345	FR I	R V R	J09
J1512.2+0202	228.06559	2.05471	0.219	2.16 ± 0.02	−0.65	30.5	121.60 ± 0.34	981.16 ± 2.50	−0.505	FR II	R V R	A20
J1516.5+0015	229.16758	0.25052	0.052	2.55 ± 0.08	−0.28	247.3	744.88 ± 0.80	2317.52 ± 5.66	−0.032	FR II	R V R	A20
J1516.8+2918	229.17330	29.30255	0.130	1.95 ± 0.15	−0.48	82.2	51.56 ± 0.25	129.43 ± 0.97	0.138	FR II	L V R	A20
J1518.6+0614	229.69053	6.23225	0.102	1.80 ± 0.16	−0.57	73.8	111.67 ± 0.27	457.98 ± 1.81	−0.183	FR I	R V R	A20
J1521.1+0421	230.34393	4.34170	0.052	2.07 ± 0.13	−0.23	247.1	180.59 ± 0.73	437.15 ± 4.50	0.140	FR I	R V R	A20
J1525.7−4334	231.30062	−43.68613	0.054	2.71 ± 0.13	−0.63	256.0	127.39 ± 0.32	545.31 ± 1.48	−0.223	FR I	R R R	B14
J1541.1+3451	235.24478	34.87312	0.233	2.59 ± 0.19	−0.59	18.7	43.39 ± 0.44	164.65 ± 0.59	−0.099	FR II	V V R	A20
J1556.1+2812	239.04852	28.19276	0.208	1.88 ± 0.18	−0.54	17.6	54.97 ± 0.23	99.14 ± 0.56	0.436	FR I	V V R	A20
J1556.6+1417	239.19008	14.26365	0.350	2.48 ± 0.18	−0.50	94.8	41.08 ± 0.28	130.26 ± 1.30	0.042	FR I	R V R	**
J1606.0+0011	241.55285	0.00755	0.059	2.71 ± 0.13	−0.63	88.9	125.87 ± 0.54	2209.39 ± 3.50	−0.924	FR I	R V R	B99
J1606.4+1814	241.56678	18.24995	0.036	1.89 ± 0.17	−0.08	344.1	183.53 ± 0.24	291.73 ± 1.51	0.517	FR I	R V R	A20
J1615.6+4712	243.9217	47.18667	0.198	2.21 ± 0.06	−0.61	86.4	80.91 ± 0.28	568.82 ± 1.48	−0.443	FR I	L V R	A20
J1636.3+7128	248.96716	71.48162	0.171	2.83 ± 0.12	−0.67	12.4	180.94 ± 0.26	274.95 ± 0.60	0.339	FR II	V V V	A98
J1643.0−7714	251.06716	−77.26355	0.043	2.51 ± 0.17	−0.70	253.5	324.72 ± 0.55	6189.11 ± 4.57	−0.967	FR II	R R R	S93
J1644.2+4546	251.08321	45.77899	0.225	1.86 ± 0.13	−0.41	27.7	61.22 ± 0.29	160.94 ± 0.67	0.133	FR II	V V R	A20
J1716.5−5631	259.09019	−56.42876	−999	2.75 ± 0.14	−1.43	37.6	7.96 ± 0.21	29.50 ± 0.55	−0.157	FR II	R R R	...
J1716.3−3421	259.09872	−34.30417	−999	2.49 ± 0.10	−0.88	14.5	82.39 ± 0.42	531.14 ± 0.63	−0.461	FR II	V V R	...
J1720.2+3824	260.04306	38.43226	0.452	2.42 ± 0.12	−0.65	108.3	151.34 ± 0.28	244.77 ± 0.85	0.614	FR I–II	L V R	A20
J1727.9−0654	261.96545	−6.96904	−999	2.62 ± 0.13	−0.81	6.6	94.00 ± 0.28	432.36 ± 0.56	−0.281	FR II	V V R	...
J1738.0+0236	264.39465	2.61400	0.177	2.82 ± 0.16	−0.57	104.8	4.68 ± 0.29	447.31 ± 1.57	−1.644	FR II	V V R	F22
J1744.8+5540	266.23587	55.70476	0.030	2.08 ± 0.16	−0.41	23.7	342.05 ± 0.28	497.13 ± 0.79	0.354	FR I	V V V	S94
J1745.0−1953	266.25430	−19.87146	−999	2.37 ± 0.17	−0.87	10.5	12.89 ± 0.35	154.66 ± 0.68	−0.766	FR II	V V R	...
J1745.6+3950	266.40730	39.85859	0.267	1.96 ± 0.11	−0.71	92.4	174.27 ± 0.21	627.52 ± 1.41	−0.058	FR I	R V R	L08
J1804.4+5249	271.09484	52.82053	0.108	1.88 ± 0.18	−0.39	35.0	4.96 ± 0.26	65.38 ± 0.87	−1.050	FR I	V V V	B14
J1812.9+4249	273.28384	42.81545	−999	2.63 ± 0.14	−0.72	29.9	21.91 ± 0.27	72.34 ± 0.95	−0.087	FR II	L V R	...
J1824.7−3243	276.23304	−32.71620	0.355	2.35 ± 0.12	−0.89	51.0	107.38 ± 0.62	3854.94 ± 4.65	−1.162	FR II	R V R	M09
J1840.3−3037	279.93490	−30.50648	−999	2.49 ± 0.13	−0.71	54.5	1.73 ± 0.30	574.01 ± 1.07	−2.245	FR II	R V R	...
J1843.7−3227	280.79364	−32.34507	−999	2.27 ± 0.15	−1.10	22.4	1.17 ± 0.34	41.39 ± 0.54	−1.261	FR II	V V R	...
J1843.4−4835	280.81091	−48.60644	0.110	2.02 ± 0.13	−0.75	204.1	650.66 ± 0.48	3568.16 ± 3.24	−0.340	FR I	R R R	J09
J1845.3+5605	281.64578	56.15798	−999	2.58 ± 0.16	−0.85	15.7	8.64 ± 0.26	41.78 ± 0.72	−0.584	FR II	V V V	...
J1918.6−7813c	290.93080	−78.19609	−999	2.62 ± 0.1	−1.16	32.6	25.48 ± 0.16	167.21 ± 0.56	−0.470	FR II	R R R	...
J1935.0−0553	293.69705	−5.89465	−999	2.64 ± 0.17	−0.80	23.1	1.71 ± 0.26	38.14 ± 0.52	−1.054	FR II	V V R	...
J1951.2−0951	297.88701	−9.92623	0.153	2.66 ± 0.17	−0.73	77.7	27.76 ± 0.29	689.28 ± 1.12	−1.053	FR I	R V R	B14
J2156.0−6942	329.27491	−69.68991	0.028	2.83 ± 0.09	−0.75	71.8	2349.29 ± 1.89	25258.90 ± 11.03	−0.705	FR II	R R R	K22
J2203.3−5009	330.58617	−50.11176	−999	2.60 ± 0.14	−0.52	56.7	2.43 ± 0.16	24.52 ± 0.47	−0.684	FR II	R R R	...
J2211.2−1325	332.85041	−13.46936	0.392	2.68 ± 0.05	−0.62	12.0	462.68 ± 0.30	1347.83 ± 0.96	0.108	FR II	V V R	P21
J2211.9+0821	333.00662	8.32125	0.483	2.51 ± 0.16	−0.66	11.4	566.01 ± 0.55	1847.77 ± 0.61	0.057	FR II	V V R	N93
J2232.3+6246	338.09526	62.82679	−999	2.55 ± 0.11	−0.68	34.5	55.55 ± 0.58	344.57 ± 2.42	−0.716	FR II	V V V	...
J2234.8−2610	338.62824	−26.15603	−999	2.09 ± 0.16	−0.63	11.4	14.65 ± 0.22	81.60 ± 0.50	−0.385	FR II	V V R	...

Table 1
(Continued)

4FGL Name [1]	R.A. [2]	Decl. [3]	z [4]	Γ_γ [5]	α [6]	LAS [7]	F_{core} [8]	F_{total} [9]	C_D [10]	Morph. [11]	Survey 12	Reference 13
J2245.9+1544	341.52080	15.74316	0.596	2.02 ± 0.06	−0.66	46.6	6.33 ± 0.19	89.01 ± 0.60	−0.679	FR II	V V R	P19
J2302.8−1841	345.76239	−18.69050	0.128	2.27 ± 0.11	−0.55	132.5	234.21 ± 0.56	1340.91 ± 3.37	−0.357	FR II	R V R	J09
J2326.9−0201	351.72406	−2.03716	0.188	2.58 ± 0.10	−0.83	101.0	155.71 ± 0.23	2400.51 ± 2.10	−0.824	FR II	V V R	A20
J2329.7−2118	352.41742	−21.22922	0.280	2.31 ± 0.08	−0.72	30.3	139.95 ± 0.34	710.42 ± 0.94	−0.250	FR I	V V R	J09
J2330.4+1230	352.54147	12.47460	0.144	2.27 ± 0.15	−0.53	60.3	122.37 ± 0.28	438.58 ± 0.89	−0.091	FR I	R V R	A20
J2341.8−2917	355.37400	−29.32083	0.051	2.27 ± 0.10	−0.38	466.8	141.46 ± 0.34	334.90 ± 1.68	0.156	FR I	R V R	J09
J2350.9−1416	357.79633	−14.26644	0.127	1.99 ± 0.15	−0.40	131.1	46.11 ± 0.40	103.67 ± 0.92	0.220	FR II	R V R	F22
J2359.3−2049	359.83139	−20.79889	0.096	1.93 ± 0.07	−0.49	23.6	72.57 ± 0.30	457.69 ± 0.58	−0.418	FR I/II	V V R	J09

Note. The column information is as follows: (1) 4FGL name; (2) R.A. of the counterpart (J2000, in degrees); (3) decl. of the counterpart (J2000, in degrees); (4) redshift (−999 for sources without redshift information); (5) γ-ray photon index in the 0.1−100 GeV energy range adopted from the 4FGL-DR4 catalog; (6) radio spectral index provided in SPECFIND; (7) largest angular size (LAS, in arcsec); (8) and (9) core and total flux densities, respectively (in millijansky); (10) core dominance; (11) morphological classification; (12) the survey which was used to estimate the LAS, core and total flux densities, in respective order; V = VLASS, F = FIRST, L = LOFAR, and R = RACS; and (13) reference for redshift.

References. A20: R. Ahumada et al. (2020); J09: D. H. Jones et al. (2009); S93: M. Stickel & H. Kuehr (1993); Z12: G. Zhao et al. (2012); J00: R. A. Jansen et al. (2000); D20: R. de Menezes et al. (2020); F22: L. Foschini et al. (2022); M96: M. J. M. Marcha et al. (1996); P17: S. Paiano et al. (2017); B09: S. Buttiglione et al. (2009); P21: H. A. Peña-Herazo et al. (2021); H12: J. P. Huchra et al. (2012); L17: D. J. Lagattuta et al. (2017); B14: M. Bilicki et al. (2014); B02: J. Bechtold et al. (2002); S06: B. Sbarufatti et al. (2006); Pa21: S. Paiano et al. (2021); F76: R. A. E. Fosbury & M. J. Disney (1976); L98: S. A. Laurent-Muehleisen et al. (1998); O08: R. L. C. Ogando et al. (2008); K18: J. K. Krogager et al. (2018); G23: A. García-Pérez et al. (2023); M11: E. K. Mahony et al. (2011); W83: B. J. Wilkes et al. (1983); G04: G. Gavazzi et al. (2004); L11: G. Lavaux & M. J. Hudson (2011); G83: S. A. Grandi (1983); W89: R. M. West & M. Tarenghi (1989); K04: B. S. Koribalski et al. (2004); B99: P. N. Best et al. (1999); A98: I. Appenzeller et al. (1998); S93: C. Simpson et al. (1993); S94: M. Stickel & H. Kuehr (1994); L08: H. Lietzen et al. (2008); M09: N. Masetti et al. (2009); K22: M. J. Koss et al. (2022); N93: K. Nilsson et al. (1993); P19: S. Paiano et al. (2019); and, **: this work.

density, on the other hand, was derived using the highest resolution survey data to ensure that the core emission is well disentangled from the extended lobes. The largest angular size was measured using the survey data in which the object under consideration was best resolved while also considering that low-resolution surveys are likely to pick the low-surface brightness extended flux density. For sources exhibiting FR II morphology, we estimated the largest angular size from the brightest pixel in the hotspot. For FR Is, on the other hand, it was computed from the 3σ outermost flux density contour level. For this purpose, the rms noise value (σ) was estimated from a nearby source-free region. Moreover, the largest angular size was computed by measuring the lengths along the jet/lobe from the core for both sides of the jet/lobe, which were then added. We caution that the true source length could be different due to projection effects, so our measurements are purely observational in nature. The core flux density was calculated by considering a circular region centered at the radio position and having the size radius as the resolution of the adopted survey. As the resolution of the RACS data significantly varies as a function of the source location, there may not be an adequate number of resolution elements across the source axis to clearly resolve the radio core. In such cases, we relied on the beam size at the location of the optical object to estimate the core flux density. In these cases, the core flux density would be an upper limit. On the other hand, the total flux density was estimated by integrating all the flux density within the outermost 3σ contour level. These parameters are provided in Table 1.

4. Discussion

The 4FGL-DR4 catalog reports 53 γ-ray emitting radio galaxies along with two steep-spectrum radio quasars. In this work, we have found 149 γ-ray sources that exhibit double-lobed radio morphology and other observational properties, such as radio spectral shape, resembling misaligned radio sources. Out of 53 known γ-ray emitting radio galaxies, 41 are present in our sample. We briefly discuss the remaining 12 objects in Appendix B.1.

An approximately threefold increase in the number of γ-ray emitting misaligned AGN is likely due to the much better sensitivity and resolution of the latest radio surveys that enabled us to identify faint extended radio structures. Furthermore, prior works have reported the detection of more γ-ray detected FR I sources than FR IIs (M. Ajello et al. 2022). This could be due to the closer proximity of the former and/or different beaming factors (see A. A. Abdo et al. 2010b; Y. Fukazawa et al. 2022). Since FR IIs are expected to have radiatively efficient accretion, their γ-ray emission might be produced due to the external Compton process, which is more sensitive to the beaming effect compared to synchrotron self-Compton mechanism (e.g., M. Sikora et al. 1994; C. D. Dermer 1995). However, optical spectroscopic observations have found several radiatively inefficient LERGs associated with FR II radio morphologies (e.g., S. Buttiglione et al. 2009), thereby raising questions on their γ-ray production mechanism. Indeed, we have found a comparable number of γ-ray emitting FR I and II radio sources in this work. The identification of a large number of γ-ray emitting FR II sources suggests that the γ-ray production mechanisms could be more complex than that explained using a standard one-zone leptonic radiative model (see D. Giannios et al. 2010; G. Migliori et al. 2011).

The core dominance is a good proxy for the orientation with respect to our line of sight (e.g., R. Morganti et al. 1997). This parameter is found to be larger for the Fermi-LAT detected misaligned AGN than their γ-ray undetected counterparts (A. A. Abdo et al. 2010b). The median logarithmic core dominance for our misaligned AGN sample is -0.302, ranging from -2.245 to 0.614 (Figure 2, panel (a)). Dividing the sources based on their optical spectral properties, we found that objects having LERG-type spectra have smaller core dominance (median $C_D = -0.245$) than those exhibiting broad emission lines (median $C_D = -0.04$, Figure 2, panel (a), where all broad emission-line objects have been listed as BLRGs). Though the derived values are comparatively higher than that noticed for γ-ray undetected radio galaxies, the observed trend is similar to that reported in previous studies (see R. Morganti et al. 1997). Furthermore, by dividing the sources based on their observed morphologies, we found that FR I sources tend to be more core-dominated (median $C_D = -0.239$) compared to FR IIs (median $C_D = -0.461$). This is consistent with the known trend for the degree of core dominance to decrease with an increase in total radio luminosity. For example, in a study of the low-luminosity B2 radio galaxies, the majority of which were FR Is, along with the more luminous 3CR radio galaxies, most of which belong to the FR II category, core dominance was found to systematically decrease over about five orders of magnitude of radio luminosity (e.g., H. R. de Ruiter et al. 1990, and references therein).

Panel (b) of Figure 2 shows the distribution of the radio power measured at rest-frame 178 MHz frequency. For this purpose, we extrapolated the observed extended flux density values of 123 sources with known redshifts to the rest-frame 178 MHz, assuming a spectral index $\alpha = -0.8$. The logarithmic median for the whole sample is 26.07 (in $\mathrm{W\,Hz^{-1}}$). Dividing the sources based on their observed FR I and II morphologies, the median values are 25.51 and 26.83, respectively. These results are aligned with the traditional threshold of $10^{26}\,\mathrm{W\,Hz^{-1}}$, with FR Is having lower luminosities. However, considering individual sources, exceptions are found in both classes, i.e., low-power FR IIs and high-power FR Is (see also B. Mingo et al. 2019).

The redshift distributions of FR I and II sources are shown in panel (c) of Figure 2, and the estimated median values are 0.09 and 0.24, respectively. As also found in earlier works, FR IIs are located farther than FR Is. Improved sensitivity must have contributed to the γ-ray detection of many FR II sources, which are, on average, located at higher redshifts. Another possibility could be the harder γ-ray spectra of FR Is making them easier to detect with Fermi-LAT (e.g., A. A. Abdo et al. 2010b). With the addition of more data, hence deeper sensitivity, more soft spectrum FR IIs have now been detected. This is evident in panel (d) of Figure 2, where we show a plot of γ-ray luminosity versus photon index considering blazars present in the 4FGL-DR4 catalog. A major fraction of the misaligned AGN tends to occupy a region of soft γ-ray spectra (photon index >2) and low luminosity. These results are consistent with recent works (see, e.g., G. Bruni et al. 2022).

Panel (e) of Figure 2 shows the Wide-field Infrared Survey Explorer (WISE) color–color diagram. Earlier works have shown that WISE colors can be used to distinguish accretion modes in jetted AGN (G. Gurkan et al. 2014). We have used the WISE color distinction reported in P. Dabhade et al. (2020) and plotted 149 γ-ray detected misaligned AGN. For a
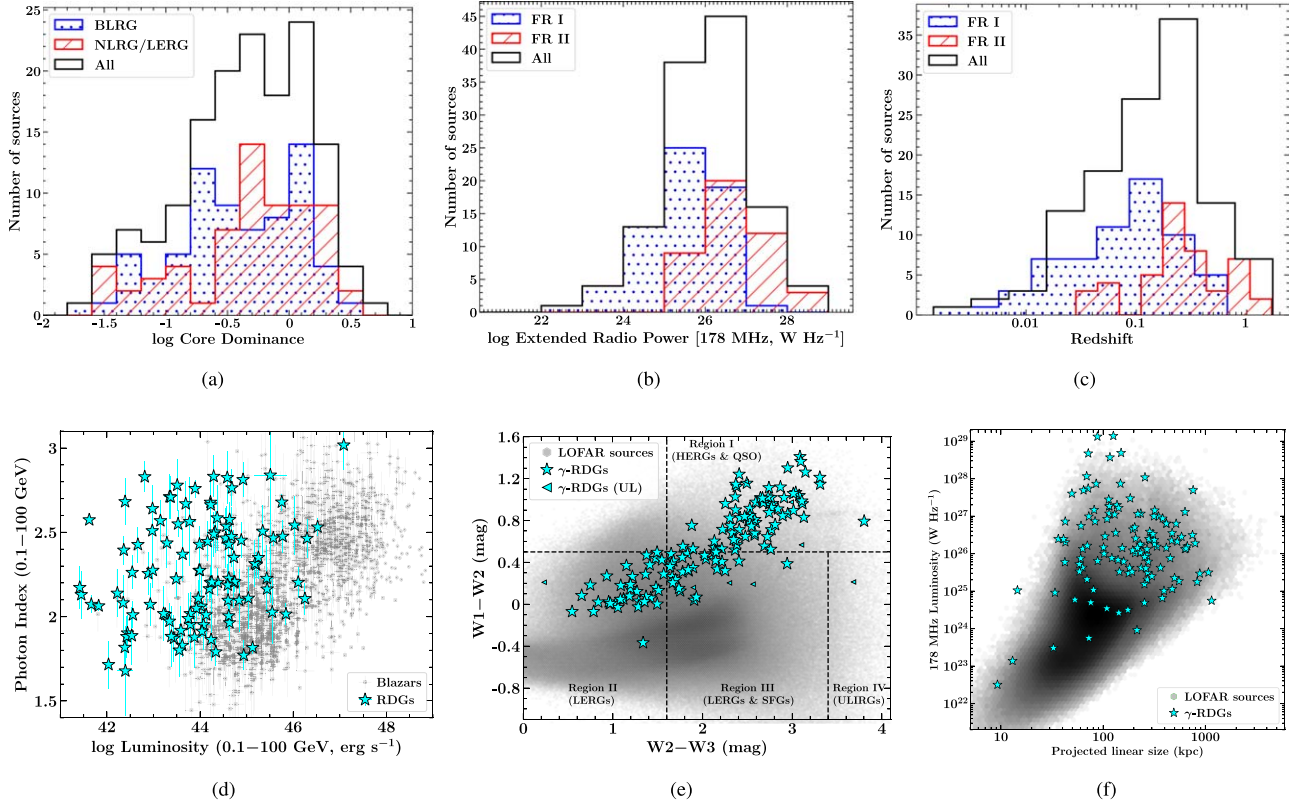
Figure 2. The histograms of the core dominance (panel (a)), radio power (panel (b)), and redshift (panel (c)) for the 149 misaligned AGN found in this work. In the top left panel, the blue-dotted and red-hatched histograms refer to objects whose optical spectra exhibit broad emission lines and host galaxy absorption features or narrow emission lines, respectively. In the top middle and right panels, these correspond to objects showing FR I and II morphologies, respectively, as found in this work. Panel (d) shows the γ-ray luminosity vs. photon index plot for Fermi-LAT detected jetted sources. The panels (e) and (f) correspond to the WISE color–color diagram and total radio power versus projected jet length plot, respectively. In all the panels, the γ-ray detected misaligned AGN are highlighted with filled cyan stars. The filled triangles shown in panel (e) refer to the upper limit in the $W3$-band magnitude. The gray data points belong to the Fermi-LAT blazars (panel (d)) and LOFAR-detected sources (panels (e) and (f)).

comparison, we have also shown the WISE colors of LOFAR-detected sources (M. J. Hardcastle et al. 2023). In this diagram, the sample of γ-ray sources mainly occupies the regions of HERGs and quasars (region I) and that of LERGs (region II). A few sources also lie in the region of LERGs and star-forming galaxies.

The power/linear size plane ($P-D$ diagram; J. E. Baldwin 1982; C. R. Kaiser et al. 1997) for LOFAR-detected objects is shown in panel (f) of Figure 2 using the data published by M. J. Hardcastle et al. (2023). To include the sample of the γ-ray detected misaligned AGN, we extrapolated their observed total flux densities to that at rest-frame 178 MHz, assuming a spectral slope of -0.8. In this diagram, the γ-ray sources tend to lie in a region of higher jet luminosity and a projected linear size spread around a few hundred kiloparsecs. The $P-D$ diagram has been extensively used to explore the evolution of radio-loud AGN; however, the location of γ-ray detected sources on this plane should be studied with the caution that they are expected to have stronger Doppler boosting effects (see M. L. Lister et al. 2015; M. J. Hardcastle et al. 2019).

5. Summary

We have carried out a radio morphological study of a sample of γ-ray emitting AGNs present in the 4FGL-DR4 catalog to identify potential misaligned jetted sources. We summarize our findings below.

1. We have identified 149 γ-ray detected misaligned AGN, significantly increasing the known sample size. This is roughly three times the previously known objects of this class, emphasizing the effectiveness of using high-resolution and sensitive radio surveys.

2. The identified sources exhibit a variety of radio morphologies, including edge-darkened (FR I), edge-brightened (FR II), hybrid, wide-angle-tailed, bent jets, and giant radio sources. This diversity indicates that γ-ray emission is not restricted to a specific radio morphology but can arise from a range of AGN structures.

3. We confirm that core dominance is a reliable indicator of the jet viewing angle. In our sample, most of the γ-ray emitting misaligned AGN have low core dominance values, suggesting that their jets are not aligned with our line of sight. Among the FR I and FR II radio sources, the former appears to be more core-dominated.

4. We found several sources with hybrid morphology (e.g., FR I on one side and FR II on the other) and complex structures (e.g., wide-angle tailed and bent jets). These findings suggest that the jet interactions with the surrounding environment can lead to diverse and complex radio structures. Since the γ-ray emission from relativistic jets is highly sensitive to the jet viewing angle, the identification of such a large number of γ-ray emitting misaligned jetted AGN raises questions on our current understanding of high-energy emission processes operating in relativistic jets.

5. Most of the γ-ray detected misaligned AGN in our sample have optical spectra dominated by host galaxy absorption features and/or narrow emission lines, consistent with the properties of misaligned jets. This reinforces the idea that γ-ray emission can be detected in AGN without the relativistic beaming seen in blazars.

6. The identification of γ-ray emitting AGN in various environments, including cluster galaxies, implies significant AGN feedback processes. These jets likely impact the intergalactic medium, influencing star formation and galaxy evolution. Deeper multiwavelength observations are needed to explore these aspects.

Appendix A
Multiwavelength Counterparts of Unidentified Gamma-Ray Sources

To determine the potential counterparts of 2430 unID, we relied upon the fact that blazars and radio galaxies are the most common type of astrophysical objects among the γ-ray sources with the known counterparts. Since jetted AGN are known to radiate across the electromagnetic spectrum, an astrophysical object detected at all accessible wavelengths is expected to be the most probable counterpart of a unID. Therefore, we first identified all X-ray detected sources lying within the 95% uncertainty regions of the optimized γ-ray positions of unIDs provided in the 4FGL-DR4 catalog. The parent sample of X-ray sources was prepared utilizing Chandra Source Catalog (I. N. Evans et al. 2010), eROSITA-DE data release 1 (A. Merloni et al. 2024), XMM-Newton serendipitous source catalog (4XMM-DR13; N. A. Webb et al. 2020), and live Swift-X-ray Point Source Catalog (P. A. Evans et al. 2023). This exercise resulted in a total of 8971 X-ray sources found within the 95% uncertainty regions of 1533 γ-ray sources. Next, we cross-matched 8971 X-ray positions with the radio sources included in the latest VLASS/RACS (depending on the source location) catalogs to determine the radio counterpart of X-ray objects. We found 637 radio and X-ray-emitting objects. Then, we cross-matched them with the WISE (E. L. Wright et al. 2010) catalog using a $5''$ search radius, which led to the identification of 489 objects also detected in the IR band. Among them, 429 are unique sources located within the 95% γ-ray positional uncertainty regions of unID. There are 47 unIDs that have more than one X-ray-radio-IR emitting objects lying within the γ-ray uncertainty ellipses. In such cases, we carefully checked their multiband parameters, e.g., flux brightness, to ascertain the most promising counterpart. The radio morphologies of these 476 most probable unID counterparts were then inspected following the procedures outlined in Section 3.

Appendix B
Notes on Interesting Objects

We briefly discuss the interesting findings about the double-lobed radio sources below, except those that are already well-studied as radio galaxies in the literature.

4FGL J0001.4−0010 or FBQS J0001−0011. This object is classified as a BL Lac in the 4FGL-DR4 catalog. However, its VLASS quick-look image reveals it to be a wide-angled-tailed (WAT) FR I source. The source has a steep radio spectrum. The Sloan Digital Sky Survey (SDSS) optical spectrum is consistent with that of a galaxy. These observations and a low core dominance suggest this source to be a misaligned AGN. There is another galaxy located at $\sim7\rlap{.}''5$ in the northeast direction and has a redshift ($z = 0.464$) similar to FBQS J0001 −0011 ($z = 0.462$). This observation indicates the γ-ray source to be located in a cluster environment. and the observed WAT-shaped radio morphology supports this possibility.

4FGL J0013.6+4051 or 4C +40.01. The VLASS image of this unclassified, lobe-dominated AGN shows a hybrid morphology. A lobe with a hotspot, similar to FR IIs, is identified in the southeast direction, whereas FR I radio morphology is seen on the opposite side. Both the VLASS and LOFAR images show diffuse emission surrounding the object, reminiscent of a fat double such as 3CR 310 (e.g.,

R. P. Kraft et al. 2012). Its overall radio spectrum is steep. The optical spectrum of the source is red and shows galaxy absorption features and only narrow emission lines (M. Stickel & H. Kuehr 1993). This object was recently proposed as a misaligned AGN by L. Foschini et al. (2022).

4FGL J0018.8+2611 or 4C +25.01. This object is a marginally core-dominated broad-line quasar. The VLASS image resolved the source into a misaligned triple structure with two edge-brightened lobes and a bright core, which has been referred to as a dog-leg structure (e.g., I. Fernini 2014, and references therein). The high-resolution image by I. Fernini (2014) shows two knots of emission toward the south, which could be part of a jet. The misaligned morphological features are also seen in the LOFAR and RACS images. This source was also studied by A. C. Gower & J. B. Hutchings (1984), who explained the observed curved shape due to the interaction of the quasar with the intergalactic medium and/or possible projection effects (see also V. K. Kapahi & D. J. Saikia 1982). The radio spectrum of the source is steep.

4FGL J0309.4−4000 or PKS 0307−402. This γ-ray source is classified as a BL Lac in the 4FGL-DR4 catalog. Its RACS image shows a complex morphology. The radio emission observed to the north of the core is likely to be associated with a different optical object ($\alpha = 47°3045020$, $\delta = -40°0194409$). A lobe-like feature seen in the southeastern direction is also found to be positionally consistent with an optical source ($\alpha = 47°3301066$, $\delta = -40°0476778$). Excluding these two features, the radio morphology of the source appears like a C-shaped/WAT structure. Such bent radio jets are often found in FR I radio galaxies, which are located in dense cluster environments. The optical spectrum of PKS 0307−402 shows host galaxy absorption features similar to that typically seen in a LERG (H. A. Peña-Herazo et al. 2021). Its overall radio spectrum is steep and the derived core dominance indicates the source to be a lobe-dominated AGN.

4FGL J0550.5−3216 or PKS 0548−322. This source is classified as a BL Lac in the 4FGL-DR4 catalog. Its optical spectrum consists of a blue non-thermal continuum along with the host galaxy absorption features (R. A. E. Fosbury & M. J. Disney 1976). R. R. J. Antonucci & J. S. Ulvestad (1984) reported the detection of a head-tail morphology, which was well resolved in the VLASS image analyzed in this work. The low-frequency observations taken with RACS also reveal this object's WAT nature and much larger diffuse emission toward the southern direction. The computed core dominance is low.

4FGL J0904.0+2724 or B2 0900+27. This distant γ-ray source exhibits broad emission lines in its optical spectrum, leading to its classification as an FSRQ. Its radio spectrum is steep. The VLASS image of this object reveals a double-lobed structure with the hotspot toward the southeastern direction being clearly visible. There is a suggestion of a jet toward the northeast, which is also seen in the Very Long Baseline Array (VLBA) observations at 7.6 GHz (L. Petrov 2021). It is moderately core-dominated and is likely to be misaligned.

4FGL J0920.2−3835 or MRC 0918−383. This object is reported as a blazar candidate of uncertain type (BCU) in the 4FGL catalog. Its RACS image shows a hybrid morphology. A bright lobe and jet emission are observed toward the northwest of the core. This feature is also resolved in the VLASS data. On the other hand, a much larger diffuse emission, similar to FR Is, is identified in the southeastern direction. This feature is not seen in the VLASS data. The northwestern jet was also

observed in the Molonglo Observatory Synthesis Telescope data taken at 843 MHz with 44″ resolution (P. A. Jones & W. B. McAdam 1992). The estimated core dominance suggests MRC 0918−383 to be a lobe-dominated AGN. The overall radio spectrum is steep. There is no published optical spectroscopic information about this object.

4FGL J0948.0−3859. The object VLASS1QLCIR J094835.22−385859.2, also known as PMN J0948−3859, is a possible counterpart of this unidentified γ-ray source. Its VLASS and RACS images show interesting radio structures. The inner jet is identified south of the core, whereas a diffuse, FR I type structure is observed in the northern direction, which is further bent toward the southwest. The overall morphology is consistent with an FR I type radio galaxy. Its radio spectrum is steep and the estimated core dominance suggests it to be a lobe-dominated AGN.

4FGL J1008.0+0028 or PKS 1005+007. This γ-ray source has been classified as a BL Lac in the 4FGL-DR4 catalog. Its VLASS image reveals a lobe-dominated, hybrid radio morphology. A lobe with a hotspot, similar to FR IIs, was seen in the northeastern direction, whereas there is a larger diffuse, plume-shaped FR I radio emission on the western side. The FIRST data shows a similar morphology along with larger scale diffuse low-surface brightness radio emission perpendicular to the jet direction. Indeed, this source has been proposed as an "X-shaped" radio galaxy (D. H. Roberts et al. 2018). The optical spectrum of PKS 1005+007 appears to be dominated by the galaxy absorption features, and the host galaxy is resolved in the Pan-STARRS i-band image.

4FGL J1121.3−0011 or MGC 0019706. This γ-ray source is classified as a BCU in the 4FGL-DR4 catalog. Its FIRST image shows a curved FR I morphology similar to WAT radio galaxies, indicating it to lie in a cluster environment (see also V. R. Eke et al. 2004; E. M. Sadler et al. 2014). The RACS data also reveals a similar radio morphology. The source was earlier imaged by P. Parma et al. (1991) in a study of dumbbell galaxies, who reported a similar structure associating the source with the brighter northwestern component of the dumbbell system. The optical spectrum of the source is similar to that seen in LERGs (A. García-Pérez et al. 2023). It has been reported as a misaligned AGN by L. Foschini et al. (2022). The derived core dominance suggests this object to be a lobe-dominated AGN and its overall radio spectrum is steep.

4FGL J1230.9+3711 or 1RXS J123124.8+371117. This object has been reported as a narrow-line radio galaxy (NLRG) with a hybrid FR I/II morphology (D. Kozieł-Wierzbowska & G. Stasinska 2011; M. Sikora et al. 2013). The LOFAR and RACS images show a lobe and a hotspot west to the core and a diffuse low-surface brightness emission eastward of the core, and thus consistent with this finding. The SDSS optical spectrum is similar to the LERG-type AGN. The overall radio spectrum of the source is steep. The computed core dominance suggests it to be a lobe-dominated AGN. It is also reported as a misaligned AGN by L. Foschini et al. (2022).

4FGL J1233.6+5027 or TXS 1231+507. This object is classified as a BL Lac in the 4FGL-DR4 catalog. The VLASS image shows edge-brightened lobes similar to FR II sources, while the lower-resolution images, especially the low-frequency LOFAR image, show plume-shaped diffuse emission on both sides. The plume on the northwestern side is more extended and bends away from the axis of the source toward the north. The LOFAR observation of TXS 1231+507 has also

been studied by U. Pajdosz-Smierciak et al. (2022), who proposed the jet reorientation as a possible explanation for the observed feature. The optical spectrum of this object is galaxy-dominated, and the radio spectrum is steep. This object has been proposed as a misaligned AGN by L. Foschini et al. (2022).

4FGL J1256.9+2736. The source VLASS1QLCIR J125724.39+272956.4, also known as NGC 4839, is the possible counterpart of this unidentified Fermi-LAT detected source. This object is reported to be the brightest cluster galaxy (BCG) in the NGC 4839 group, which is merging with the Coma cluster (see S.-A. Oh et al. 2023). Its VLASS image shows diffuse, bipolar radio emission similar to FR I radio galaxies. The source is also resolved in the FIRST and LOFAR data sets. The latter shows a C-shaped radio structure along with a low-surface brightness emission toward the southwestern direction. The SDSS optical spectrum comprises absorption features arising from the host galaxy stellar population. It is a lobe-dominated AGN and has a steep radio spectrum.

4FGL J1326.2+4115 or IVS B1323+415. This source is classified as a BL Lac in the 4FGL-DR4 catalog. Its LOFAR data reveals curved jets hinting at a C-shaped FR I structure reminiscent of a WAT radio galaxy. Similar results are obtained by examining the FIRST and RACS data sets. The SDSS optical spectrum of this source is similar to that of a LERG or an NLRG. It is a moderately core-dominated AGN with a flat radio spectrum.

4FGL J1327.0+3154 or 4C +32.44B. The optical spectrum of this γ-ray emitting BCU shows bright, narrow emission lines on top of a red continuum and host galaxy absorption features. The VLASS image of this object shows it to be lobe-dominated, with an overall structure reminiscent of a WAT source. There is a prominent hotspot toward the south, with low-surface brightness diffuse emission appearing to surround the source. Similar features were also seen in the FIRST and LOFAR data. Its radio spectrum is steep. This object has been reported as a BCG by T. Szabo et al. (2011), consistent with its bent morphology being due to the cluster environment.

4FGL J1340.1+3857 or 3C 288. This γ-ray source is classified as a BCU in the 4FGL-DR4 catalog. It has shown edge-darkened morphology in VLA observations, though its 1.5 GHz radio power (2.5×10^{33} erg cm^{-2} s^{-1} Hz^{-1}) indicates it to be an FR II radio source. A. H. Bridle et al. (1989) reported the identification of a jet and a counterjet near the radio core and extended radio wings connected with the radio lobes. Their $0\rlap{.}{''}6$ resolution image shows edge brightening in the inner lobes, which merge with the wings. A WAT-shaped radio morphology suggests it may be associated with a cluster of galaxies. The optical spectrum of this object is typical of a LERG (S. Buttiglione et al. 2009). It is a lobe-dominated AGN with a steep radio spectrum.

4FGL J1341.2+3958 or RBS 1302. This γ-ray detected object is classified as a BL Lac in the 4FGL-DR4 catalog. It exhibits a complex morphology in the LOFAR data. A diffuse FR I jet is seen in the northeastern direction, which is connected with a large extended low-surface brightness radio emission almost throughout its length. The source is partially resolved in the FIRST and RACS data sets showing similar radio structures. It is consistent with a WAT whose tails appear superposed. The SDSS optical spectrum shows host galaxy absorption features. The estimated core dominance hints that

RBS 1302 is a lobe-dominated AGN. The overall radio spectrum is steep. This object is identified as a low-power radio galaxy by Y.-T. Lin et al. (2018).

4FGL J1342.7+0505 or 4C +05.57. This lobe-dominated source is classified as a BL Lac in the 4FGL-DR4 catalog. It has also been identified as a narrow-line radio galaxy (M. Sikora et al. 2013). The VLASS image of this object shows a complex radio morphology. There is a jet spewing southward of the radio core with a lobe/knot positionally consistent with an optical object located at $\sim5''$. At milliarcsecond scale, the direction of the jet probed by VLBA is the same. This observation indicates that the secondary object could be the optical jet rather than a separate astrophysical object. Furthermore, a "Z"-shaped FR I radio morphology is seen on a large scale. The SDSS optical spectrum of 4C +05.57 is dominated by the strong, narrow emission lines and host galaxy absorption features. This object has been proposed as a misaligned AGN by L. Foschini et al. (2022).

4FGL J1346.5+5330 or RBS 1310. This unclassified Fermi-LAT detected AGN has revealed a complex radio structure in the LOFAR cutout image. Closer to the core, bipolar radio jets are seen in the east–west directions. However, the large-scale jet appears to be oriented in northeastern and southwestern directions. The inner structure is also resolved in the VLASS and FIRST data sets. This "S"-shaped morphology has also been reported by Y.-X. Liu et al. (2019). U. Pajdosz-Smierciak et al. (2022) explained the observed morphology due to possible jet reorientation. The source exhibits a steep radio spectrum and the computed core dominance indicates it to be a lobe-dominated AGN. Its SDSS optical spectrum has revealed broad emission lines along with host galaxy absorption features.

4FGL J1402.6+1600 or 4C +16.39. This object is classified as a BL Lac in the 4FGL-DR4 catalog. However, its optical spectrum shows a blue continuum with narrow emission lines and host galaxy absorption features. The radio structure of the source revealed by VLASS consists of two bright lobes with hotspots, a core, and a jet toward the eastern direction of the core. The calculated core dominance suggests the source to be marginally lobe-dominated, and the overall radio spectrum is steep. The FIRST data exhibits similar features along with larger low-surface brightness emission surrounding the object. R. R. J. Antonucci & J. S. Ulvestad (1985) analyzed the VLA data of 4C +16.39 and reported the identification of triple radio structure, i.e., a core and double lobes, with complex morphology. Higher-resolution observations show the jet to be curved, with the outer prominent knot having a magnetic field structure, suggesting interaction with the external environment (D. J. Saikia et al. 1987).

4FGL J1413.1−6519 or Circinus galaxy. This source is the nearest Seyfert 2 galaxy and has been extensively studied. Its RACS image shows an X-shaped radio structure. Overplotting the RACS contours on the Dark Energy Camera image, the brighter emission, likely to be produced due to an edge-brightened jet, appears perpendicular to the galaxy disk. On the other hand, the fainter radio emission, which is aligned to the galaxy disk, possibly originated from starburst activities (e.g., M. Elmouttie et al. 1998). Its overall radio spectrum is steep.

4FGL J1615.6+4712 or TXS 1614+473. This source is classified as an FSRQ in the 4FGL-DR4 catalog. However, its SDSS optical spectrum is found to be similar to a LERG with

no visible broad emission lines. The FIRST image of this source shows a complex radio morphology, suggestive of a WAT structure where the tails of emission appear merged. Moreover, the tail of extended radio emission in the northeastern direction is also visible in the LOFAR data. H. Miraghaei & P. N. Best (2017) reported this source to be an FR I radio galaxy based on the FIRST data. It is reported as a misaligned AGN by L. Foschini et al. (2022). It is a lobe-dominated AGN with a steep radio spectrum.

4FGL J1720.2+3824 or SDSS J172010.33+382556.1. This γ-ray source is reported as a BCU in the 4FGL-DR4 catalog. It exhibits a hybrid morphology in the LOFAR image. An FR II jet, including a radio knot and a lobe, is identified in the southwestern direction. A diffuse FR I lobe is observed in the northwestern direction, giving an impression of an overall C-shaped radio structure. The source is partially resolved in the RACS data, whereas the FIRST image shows only the southwestern jet. It is a core-dominated AGN and has a steep radio spectrum. The SDSS optical spectrum is similar to Type 2 Seyfert galaxies. L. Foschini et al. (2022) have suggested this object to be a misaligned AGN.

4FGL J1745.6+3950 or RX J1745.5+3951. Originally classified as a BL Lac, this source is also proposed as a BCG (H. Lietzen et al. 2008). Its optical spectrum exhibits strong host galaxy absorption features. The LOFAR image of this source reveals a WAT-shaped radio morphology with eastern and western jets bent southward. This object is moderately lobe-dominated and has a steep radio spectrum.

4FGL J1840.3−3037 or PKS 1836−305. This Fermi-LAT detected BCU exhibits a triple radio structure in the VLASS data with a weak core. A radio-emitting knot is also resolved toward the southeastern side. The RACS image shows the double-lobed structure with an FR II morphology and prominent wings of emission reminiscent of an X-shaped source. The estimated core dominance parameter indicates the source to be a lobe-dominated AGN. The overall radio spectrum is steep.

4FGL J1951.2−0951 or PKS 1948−10. This object is classified as a BCU in the 4FGL-DR4 catalog due to the lack of optical spectroscopic information. It exhibits an inverted "C"-shaped FR I morphology in the VLASS data, indicating it to be a possible WAT radio galaxy. This source is a lobe-dominated AGN with a steep radio spectrum.

4FGL J2211.9+0821 or PKS 2209+08. This well-studied quasar is known to exhibit kiloparsec-scale optical and X-ray jets (e.g., P. Breiding et al. 2017). Its VLASS image exhibits a double-lobed FR II morphology. It is marginally core-dominated, and the overall radio spectrum is steep. J. R. A. Hooimeyer et al. (1992) reported the VLA observation of the source, which resolved it into a prominent core and a bright jet, including knots and hotspots, extending southward. A counter-lobe with a hotspot was also seen.

4FGL J2359.3−2049 or TXS 2356−210. This γ-ray detected BL Lac object was earlier studied by V. K. Kapahi et al. (1998), who reported the identification of a triple radio structure. The VLASS image of this source exhibits a bright FR II lobe in the northeastern direction, while a higher-resolution image is required to clarify the structure on the southwestern side. It is a lobe-dominated object whose measured radio spectral index lies at the boundary of the flat/steep spectrum definition.

B.1. Missing Gamma-Ray Emitting Radio Galaxies

The 12 γ-ray emitting radio galaxies present in the 4FGL-DR4 catalog are missing from our sample of double-lobed radio sources. For most of them, the primary reason is the non-detection of the bipolar extended radio emission in the considered survey data and/or their observed properties, such as $C_{\rm D}$ and radio spectral index, not qualifying the adopted criteria. We discuss them below.

4FGL J0312.9+4119 or B3 0309+411B. This object was first reported as a giant radio galaxy using 327 MHz observations taken with Westerbork Synthesis Radio Telescope (A. G. de Bruyn 1989). They identified rapid flux variability at cm wavelengths and a core-dominated emission, indicating a small viewing angle of the jet axis. The VLASS quick-look image of this object is affected by artifacts, possibly due to bright core emission. The RACS data taken at $\sim$1.4 GHz reveals a core-jet structure. This source is not present in the footprints of other surveys considered in this work.

4FGL J0319.8+4130 or NGC 1275. It is an asymmetrical FR I radio source located in the Perseus cluster (A. Pedlar et al. 1990). Its VLASS quick-look images are affected by artifacts, possibly due to bright core emission. The RACS 1.4 GHz data shows a compact radio emission with no obvious extended structure. The source is not present in the footprints of other surveys considered in this work.

4FGL J0433.0+0522 or 3C 120. This object has been reported as a broad-line FR I radio galaxy (e.g., F. N. Owen & R. A. Laing 1989). It has a high core dominance ($C_{\rm D} = 0.691$), and the overall radio spectrum is flat. Its optical spectrum is also similar to Type 1 broad-line quasars. Since none of the observables support its misaligned nature, this object has not appeared in our sample.

4FGL J0931.9+6737 or NGC 2892. The γ-ray source 4FGL J0931.9+6737 has been associated with the radio galaxy NGC 2892. However, the coordinates of the counterpart given in the 4FGL-DR4 catalog refer to a BL Lac object, which is about 5′ away from NGC 2892. We found that NGC 2892 lies outside of the 95% uncertainty region of the γ-ray position reported in the 4FGL-DR4 catalog, hence is not the correct counterpart of 4FGL J0931.9+6737. L. Foschini et al. (2022) also arrived at the same conclusion about this γ-ray source.

4FGL J1149.0+5924 or NGC 3894. This source has been identified as a compact symmetric object hosting twin parsec-scale jets (S. Kiehlmann et al. 2024). Its VLASS cutout images are affected by artifacts, and it is barely resolved in the LOFAR Data. It is extremely core-dominated ($C_{\rm D} = 1.90$) and has an inverted flat radio spectrum ($\alpha = 0.16$). Therefore, this source did not pass the selection criteria adopted in this work to identify misaligned AGN.

4FGL J1449.5+2746 or B2 1447+27. This source exhibited a compact core morphology in VLASS, FIRST, and RACS images. We could not find any published radio image of this object where a double-lobed morphology was identified. Moreover, H. R. de Ruiter et al. (1986) reported B2 1447+27 to consist of a single component with an angular size of 3.6×1.4 arcsec^2. Therefore, it has not entered our sample.

4FGL J1530.3+2709 or LEDA 55267 and 4FGL J1628.8+2529 or LEDA 58287. These objects are identified as FR 0 radio galaxies, which are objects having optical properties similar to FR Is but lack extended radio jets (R. D. Baldi et al. 2018; V. S. Paliya 2021; M. Pannikkote et al. 2023).

4FGL J1724.2−6501 or NGC 6328. The radio properties of this object were studied by S. J. Tingay et al. ([1997](#)), who reported it to be a GHz peaked-spectrum object. The milliarcsecond-scale radio observations indicated this source to be a newly born compact symmetric object (S. J. Tingay et al. [1997](#)). NGC 6328 has a compact morphology in the RACS observation, and no extended emission was observed.

4FGL J2227.9-3031 or PKS 2225−308. P. A. Jones & W. B. McAdam ([1992](#)) reported the detection of a double source using the Molonglo Observatory Synthesis Telescope at 843 MHz and 44″ resolution. However, the RACS image of this source revealed a compact radio object. There is a nearby galaxy (LEDA 192291) that exhibits a head-tail morphology and was also reported by R. D. Ekers et al. ([1989](#)). The VLASS data showed a slightly resolved radio jet in the northwest direction.

4FGL J1630.6+8234 or NGC 6251. This object is a giant radio galaxy identified using MHz frequency observations (see P. C. Waggett et al. [1977](#)). Its VLASS quick-look image is dominated by the bright, compact core with no clear extended radio structure. This source does not lie in the footprints of other considered surveys.

4FGL J2333.9−2343 or PKS 2331−240. This is a giant radio galaxy with a blazar nucleus, and thus, it is probably the best example of jet bending (e.g., L. Hernández-García et al. [2017](#)). Its RACS cutout image has revealed a bright, compact core and two lobes with the bridge emission remaining undetected (see also, G. Bruni et al. [2020](#)). It has a high core dominance ($C_D = 1.016$) and has an inverted and flat radio spectrum ($\alpha = 0.13$). Therefore, this source did not pass the selection criteria adopted in this work to identify misaligned AGN.

ORCID iDs

Vaidehi S. Paliya ⓘ https://orcid.org/0000-0001-7774-5308
D. J. Saikia ⓘ https://orcid.org/0000-0002-4464-8023
Alberto Domínguez ⓘ https://orcid.org/0000-0002-3433-4610
C. S. Stalin ⓘ https://orcid.org/0000-0002-4998-1861

References

Abbott, T. M. C., Adamów, M., Aguena, M., et al. 2021, ApJS, 255, 20
Abdo, A. A., Ackermann, M., Ajello, M., et al. 2010a, Sci, 328, 725
Abdo, A. A., Ackermann, M., Ajello, M., et al. 2010b, ApJ, 720, 912
Abdollahi, S., Acero, F., Baldini, L., et al. 2022, ApJS, 260, 53
Ahumada, R., Allende Prieto, C., Almeida, A., et al. 2020, ApJS, 249, 3
Ajello, M., Baldini, L., Ballet, J., et al. 2022, ApJS, 263, 24
Angioni, R., Ros, E., Kadler, M., et al. 2019, A&A, 627, A148
Antonucci, R. R. J., & Ulvestad, J. S. 1984, Natur, 308, 617
Antonucci, R. R. J., & Ulvestad, J. S. 1985, ApJ, 294, 158
Appenzeller, I., Thiering, I., Zickgraf, F. J., et al. 1998, ApJS, 117, 319
Baldi, R. D., Capetti, A., & Massaro, F. 2018, A&A, 609, A1
Baldwin, J. E. 1982, in IAU Symp. 97, Extragalactic Radio Sources, ed.
    D. S. Heeschen & C. M. Wade, 21
Ballet, J., Bruel, P., Burnett, T. H., Lott, B. & The Fermi-LAT collaboration
    2023, arXiv:2307.12546
Bechtold, J., Dobrzycki, A., Wilden, B., et al. 2002, ApJS, 140, 143
Best, P. N., & Heckman, T. M. 2012, MNRAS, 421, 1569
Best, P. N., Rottgering, H. J. A., & Lehnert, M. D. 1999, MNRAS, 310, 223
Bilicki, M., Jarrett, T. H., Peacock, J. A., Cluver, M. E., & Steward, L. 2014,
    ApJS, 210, 9
Breiding, P., Meyer, E. T., Georganopoulos, M., et al. 2017, ApJ, 849, 95
Bridle, A. H., Fomalont, E. B., Byrd, G. G., & Valtonen, M. J. 1989, AJ,
    97, 674
Bruni, G., Bassani, L., Persic, M., et al. 2022, MNRAS, 513, 886
Bruni, G., Panessa, F., Bassani, L., et al. 2020, MNRAS, 494, 902
Buttiglione, S., Capetti, A., Celotti, A., et al. 2009, A&A, 495, 1033

Chambers, K. C., Magnier, E. A., Metcalfe, N., et al. 2016, arXiv:1612.05560
Chen, Y., Gu, Q., Fan, J., et al. 2023, ApJS, 265, 60
Chen, Y. Y., Zhang, X., Zhang, H. J., & Yu, X. L. 2015, MNRAS, 451, 4193
Chiaro, G., La Mura, G., Dominguez, A., & Bisogni, S. 2020, JHEAp, 27, 77
Condon, J. J., & Broderick, J. J. 1988, AJ, 96, 30
Dabhade, P., Mahato, M., Bagchi, J., et al. 2020, A&A, 642, A153
Dabhade, P., Saikia, D. J., & Mahato, M. 2023, JApA, 44, 13
de Bruyn, A. G. 1989, A&A, 226, L13
de Menezes, R., Amaya-Almazán, R. A., Marchesini, E. J., et al. 2020,
    Ap&SS, 365, 12
de Ruiter, H. R., Parma, P., Fanti, C., & Fanti, R. 1986, A&AS, 65, 111
de Ruiter, H. R., Parma, P., Fanti, C., & Fanti, R. 1990, A&A, 227, 351
Dermer, C. D. 1995, ApJL, 446, L63
Di Mauro, M., Calore, F., Donato, F., Ajello, M., & Latronico, L. 2014, ApJ,
    780, 161
Duchesne, S. W., Grundy, J. A., Heald, G. H., et al. 2024, PASA, 41, e003
Eke, V. R., Baugh, C. M., Cole, S., et al. 2004, MNRAS, 348, 866
Ekers, R. D., Wall, J. V., Shaver, P. A., et al. 1989, MNRAS, 236, 737
Elmouttie, M., Haynes, R. F., Jones, K. L., Sadler, E. M., & Ehle, M. 1998,
    MNRAS, 297, 1202
Evans, I. N., Primini, F. A., Glotfelty, K. J., et al. 2010, ApJS, 189, 37
Evans, P. A., Page, K. L., Beardmore, A. P., et al. 2023, MNRAS, 518, 174
Fanaroff, B. L., & Riley, J. M. 1974, MNRAS, 167, 31P
Fernini, I. 2014, ApJS, 212, 19
Fosbury, R. A. E., & Disney, M. J. 1976, ApJL, 207, L75
Foschini, L., Lister, M. L., Andernach, H., et al. 2022, Univ, 8, 587
Fukazawa, Y., Matake, H., Kayanoki, T., Inoue, Y., & Finke, J. 2022, ApJ,
    931, 138
Fukazawa, Y., Shiki, K., Tanaka, Y., et al. 2018, ApJ, 855, 93
García-Pérez, A., Peña-Herazo, H. A., Massaro, F., et al. 2023, AJ, 165, 127
Gavazzi, G., Zaccardo, A., Sanvito, G., Boselli, A., & Bonfanti, C. 2004,
    A&A, 417, 499
Giannios, D., Uzdensky, D. A., & Begelman, M. C. 2010, MNRAS, 402, 1649
Gopal-Krishna, W. P. J. 2000, A&A, 363, 507
Gordon, Y. A., Rudnick, L., Andernach, H., et al. 2023, ApJS, 267, 37
Gower, A. C., & Hutchings, J. B. 1984, AJ, 89, 1658
Grandi, P., Capetti, A., & Baldi, R. D. 2016, MNRAS, 457, 2
Grandi, P., Torresi, E., & Stanghellini, C. 2012, ApJL, 751, L3
Grandi, S. A. 1983, MNRAS, 204, 691
Gurkan, G., Hardcastle, M. J., & Jarvis, M. J. 2014, MNRAS, 438, 1149
Hardcastle, M. J., Horton, M. A., Williams, W. L., et al. 2023, A&A, 678, A151
Hardcastle, M. J., Williams, W. L., Best, P. N., et al. 2019, A&A, 622, A12
Harwood, J. J., Vernstrom, T., & Stroe, A. 2020, MNRAS, 491, 803
Healey, S. E., Romani, R. W., Taylor, G. B., et al. 2007, ApJS, 171, 61
Heckman, T. M., & Best, P. N. 2014, ARA&A, 52, 589
Helfand, D. J., White, R. L., & Becker, R. H. 2015, ApJ, 801, 26
Hernández-García, L., Panessa, F., Giroletti, M., et al. 2017, A&A, 603, A131
Hooimeyer, J. R. A., Schilizzi, R. T., Miley, G. K., & Barthel, P. D. 1992,
    A&A, 261, 25
Huchra, J. P., Macri, L. M., Masters, K. L., et al. 2012, ApJS, 199, 26
Ishwara-Chandra, C. H., & Saikia, D. J. 1999, MNRAS, 309, 100
Ivezić, Ž., Menou, K., Knapp, G. R., et al. 2002, AJ, 124, 2364
Jansen, R. A., Fabricant, D., Franx, M., & Caldwell, N. 2000, ApJS, 126, 331
Jones, D. H., Read, M. A., Saunders, W., et al. 2009, MNRAS, 399, 683
Jones, P. A., & McAdam, W. B. 1992, ApJS, 80, 137
Kaiser, C. R., Dennett-Thorpe, J., & Alexander, P. 1997, MNRAS, 292, 723
Kapahi, V. K., Athreya, R. M., van Breugel, W., McCarthy, P. J., &
    Subrahmanya, C. R. 1998, ApJS, 118, 275
Kapahi, V. K., & Saikia, D. J. 1982, JApA, 3, 465
Kiehlmann, S., Lister, M. L., Readhead, A. C. S., et al. 2024, ApJ, 961, 240
Koribalski, B. S., Staveley-Smith, L., Kilborn, V. A., et al. 2004, AJ, 128, 16
Koss, M. J., Ricci, C., Trakhtenbrot, B., et al. 2022, ApJS, 261, 2
Kozieł-Wierzbowska, D., & Stasinska, G. 2011, MNRAS, 415, 1013
Kraft, R. P., Birkinshaw, M., Nulsen, P. E. J., et al. 2012, ApJ, 749, 19
Krogager, J. K., Gupta, N., Noterdaeme, P., et al. 2018, ApJS, 235, 10
Lacy, M., Baum, S. A., Chandler, C. J., et al. 2020, PASP, 132, 035001
Lagattuta, D. J., Mould, J. R., Forbes, D. A., et al. 2017, ApJ, 846, 166
Laurent-Muehleisen, S. A., Kollgaard, R. I., Ciardullo, R., et al. 1998, ApJS,
    118, 127
Lavaux, G., & Hudson, M. J. 2011, MNRAS, 416, 2840
Lietzen, H., Nilsson, K., Takalo, L. O., et al. 2008, A&A, 482, 771
Lin, Y.-T., Huang, H.-J., & Chen, Y.-C. 2018, AJ, 155, 188
Lister, M. L., Aller, M. F., Aller, H. D., et al. 2015, ApJL, 810, L9
Liu, Y.-X., Xu, H.-G., Zheng, D.-C., et al. 2019, RAA, 19, 127
Mahony, E. K., Sadler, E. M., Croom, S. M., et al. 2011, MNRAS, 417, 2651
Marcha, M. J., Caccianiga, A., Browne, I. W. A., & Jackson, N. 2001,
    MNRAS, 326, 1455

Marcha, M. J. M., Browne, I. W. A., Impey, C. D., & Smith, P. S. 1996, MNRAS, 281, 425
Masetti, N., Parisi, P., Palazzi, E., et al. 2009, A&A, 495, 121
Massaro, F., Giroletti, M., D'Abrusco, R., et al. 2014, ApJS, 213, 3
Merloni, A., Lamer, G., Liu, T., et al. 2024, A&A, 682, A34
Migliori, G., Grandi, P., Torresi, E., et al. 2011, A&A, 533, A72
Mingo, B., Croston, J. H., Best, P. N., et al. 2022, MNRAS, 511, 3250
Mingo, B., Croston, J. H., Hardcastle, M. J., et al. 2019, MNRAS, 488, 2701
Miraghaei, H., & Best, P. N. 2017, MNRAS, 466, 4346
Morganti, R., Oosterloo, T. A., Reynolds, J. E., Tadhunter, C. N., & Migenes, V. 1997, MNRAS, 284, 541
Nilsson, K., Valtonen, M. J., Kotilainen, J., & Jaakkola, T. 1993, ApJ, 413, 453
Ogando, R. L. C., Maia, M. A. G., Pellegrini, P. S., & da Costa, L. N. 2008, AJ, 135, 2424
Oh, S.-A., Lee, M. G., & Jang, I. S. 2023, ApJ, 944, 51
Owen, F. N., & Laing, R. A. 1989, MNRAS, 238, 357
Paiano, S., Falomo, R., Franceschini, A., Treves, A., & Scarpa, R. 2017, ApJ, 851, 135
Paiano, S., Falomo, R., Treves, A., Franceschini, A., & Scarpa, R. 2019, ApJ, 871, 162
Paiano, S., Falomo, R., Treves, A., et al. 2021, MNRAS, 504, 3338
Pajdosz-Smierciak, U., Smierciak, B., & Jamrozy, M. 2022, MNRAS, 514, 2122
Paliya, V. S. 2021, ApJL, 918, L39
Paliya, V. S., Saikia, D. J., & Stalin, C. S. 2023, MNRAS, 520, L33
Pannikkote, M., Paliya, V. S., & Saikia, D. J. 2023, ApJ, 957, 73
Parma, P., de Ruiter, H. R., & Cameron, R. A. 1991, AJ, 102, 1960
Pedlar, A., Ghataure, H. S., Davies, R. D., et al. 1990, MNRAS, 246, 477
Peña-Herazo, H. A., Paggi, A., García-Pérez, A., et al. 2021, AJ, 162, 177
Petrov, L. 2021, AJ, 161, 14

Roberts, D. H., Saripalli, L., Wang, K. X., et al. 2018, ApJ, 852, 47
Sadler, E. M., Ekers, R. D., Mahony, E. K., Mauch, T., & Murphy, T. 2014, MNRAS, 438, 796
Saikia, D. J. 2022, JApA, 43, 97
Saikia, D. J., Salter, C. J., Neff, S. G., et al. 1987, MNRAS, 228, 203
Saikia, D. J., Thomasson, P., Jackson, N., Salter, C. J., & Junor, W. 1996, MNRAS, 282, 837
Sbarufatti, B., Falomo, R., Treves, A., & Kotilainen, J. 2006, A&A, 457, 35
Shimwell, T. W., Hardcastle, M. J., Tasse, C., et al. 2022, A&A, 659, A1
Sikora, M., Begelman, M. C., & Rees, M. J. 1994, ApJ, 421, 153
Sikora, M., Stasińska, G., Kozieł-Wierzbowska, D., Madejski, G. M., & Asari, N. V. 2013, ApJ, 765, 62
Simpson, C., Clements, D. L., Rawlings, S., & Ward, M. 1993, MNRAS, 262, 889
Stecker, F. W., Shrader, C. R., & Malkan, M. A. 2019, ApJ, 879, 68
Stein, Y., Vollmer, B., Boch, T., et al. 2021, A&A, 655, A17
Stickel, M., & Kuehr, H. 1993, A&AS, 100, 395
Stickel, M., & Kuehr, H. 1994, A&AS, 103, 349
Szabo, T., Pierpaoli, E., Dong, F., Pipino, A., & Gunn, J. 2011, ApJ, 736, 21
Tingay, S. J., Jauncey, D. L., Reynolds, J. E., et al. 1997, AJ, 113, 2025
Urry, C. M., & Padovani, P. 1995, PASP, 107, 803
Waggett, P. C., Warner, P. J., & Baldwin, J. E. 1977, MNRAS, 181, 465
Webb, N. A., Coriat, M., Traulsen, I., et al. 2020, A&A, 641, A136
West, R. M., & Tarenghi, M. 1989, A&A, 223, 61
Wilkes, B. J., Wright, A. E., Jauncey, D. L., & Peterson, B. A. 1983, PASA, 5, 2
Wright, E. L., Eisenhardt, P. R. M., Mainzer, A. K., et al. 2010, AJ, 140, 1868
Zhao, G., Zhao, Y.-H., Chu, Y.-Q., Jing, Y.-P., & Deng, L.-C. 2012, RAA, 12, 723